

Molecular hydrogen, deuterium and metal abundances in the damped Ly α system at $z_{\text{abs}} = 3.025$ toward QSO 0347–3819 ¹

Sergei A. Levshakov^{2,3}, Miroslava Dessauges-Zavadsky^{4,5}, Sandro D’Odorico⁴,
and

Paolo Molaro⁶

ABSTRACT

We have detected in high resolution spectra of the quasar Q0347–3819 obtained with the UVES spectrograph at the VLT/Kueyen telescope over 80 absorption features in the Lyman and Werner H₂ bands at the redshift of a damped Ly α system at $z_{\text{abs}} = 3.025$. At the same redshift, numerous absorption lines of atoms and low ions (H I, D I, C II, C II*, N I, O I, Si II, P II, Ar I, Cr II, Fe II, and Zn II) were identified. The $z_{\text{abs}} = 3.025$ system spans over $\sim 80 \text{ km s}^{-1}$ and exhibits a multicomponent velocity structure in the metal lines. The main component at $z_{\text{abs}} = 3.024855$ shows a total H₂ column density $N(\text{H}_2) = (4.10 \pm 0.21) \times 10^{14} \text{ cm}^{-2}$ and a fractional molecular abundance $f_{\text{H}_2} = (1.94 \pm 0.10) \times 10^{-6}$ derived from the H₂ lines arising from J = 0 to 5 rotational levels of the ground electronic-vibrational state. In the second strong component at $z_{\text{abs}} = 3.024684$ we were able to set a stringent upper limit to f_{H_2} of 3.3×10^{-9} (3σ c.l.). The population of the J levels can be represented by a single excitation temperature of $T_{\text{ex}} = 825 \pm 110 \text{ K}$. The ortho:para-H₂ ratio equals 3.1 ± 0.3 . This ratio is comparable to that calculated from hot H₂ formation upon grain surfaces (ortho:para-H₂ = 3:1), but is higher than the ‘freeze-out’ quantity (ortho:para-H₂ = 1:4) predicted for cosmological epochs at $z < 20$, implying recent formation of the hydrogen molecules following photo-dissociation of pristine H₂. In the main component the properties of the neutral atoms and low ions can be described with the same broadening parameter $b \simeq 3 \text{ km s}^{-1}$ of the H₂ cloud. The rate at which UV photons are absorbed in the Lyman and Werner bands is found to be $\beta_0 \simeq 2 \times 10^{-9} \text{ s}^{-1}$. Taking into account that similar β_0 values are observed in the Galactic diffuse molecular clouds, it shows that the UV radiation fields in the DLA and in the MW are very much alike. We also found the H₂ formation rate of $R n_{\text{H}} \simeq 3 \times 10^{-16} \text{ s}^{-1}$ at $z_{\text{abs}} = 3.025$ which is consistent with observations in the Galactic disk diffuse clouds where n_{H_2} is low. Comparing the relative rotational population ratios of H₂ with the measured C II*/C II ratio, we can infer that $n_{\text{H}} \simeq 6 \text{ cm}^{-3}$ in the main component, which gives a size of $D \simeq 14 \text{ pc}$ along the line of sight. The mean value of the dust-to-gas ratio estimated for the whole $z_{\text{abs}} = 3.025$ system from the [Cr/Zn] ratio is equal to $\tilde{k} = 0.032 \pm 0.005$ (in units of the mean Galactic ISM value). For the first time we unambiguously reveal a pronounced [α -element/iron-peak] enhancement of [O,Si/Zn] = 0.6 ± 0.1 (6σ c.l.) at high redshift. The simultaneous analysis of metal and hydrogen lines leads to D/H = $(3.75 \pm 0.25) \times 10^{-5}$. This value is consistent with standard big bang nucleosynthesis if the baryon-to-photon ratio, η , lies within the range $4.37 \times 10^{-10} \lesssim \eta \lesssim 5.32 \times 10^{-10}$, implying $0.016 \lesssim \Omega_{\text{b}} h_{100}^2 \lesssim 0.020$.

Subject headings: cosmology: observations — line: identification — quasars: absorption lines — quasars: abundances — quasars: individual (Q0347–3819)

1. Introduction

Molecular hydrogen H_2 , being the most abundant molecular species in the universe, plays a central role in star formation processes both at low and high redshifts (e.g., Shull & Beckwith 1982). The H_2 molecule is known to be an important coolant for gravitational collapse of hydrogen clouds at $T \sim 1000$ K. Fractional abundances of H_2 in interstellar H I regions were calculated first by Gould & Salpeter (1963) and by Hollenbach, Werner, & Salpeter (1971). They predicted the fractional abundance of molecular hydrogen $f_{\text{H}_2} \simeq 10^{-3}$, where $f_{\text{H}_2} = 2n_{\text{H}_2}/(n_{\text{H}} + 2n_{\text{H}_2})$ for a standard galactic disk cloud with $n_{\text{H}} \simeq 10 \text{ cm}^{-3}$, gas temperature of about 100 K, and the optical depth to the cloud center due to dust grains $\tau_{\text{g}} \simeq 0.1$.

The first detection of H_2 in the ISM was performed by Carruthers (1970) with a rocket-borne ultraviolet spectrometer. Later, after the launch of the *Copernicus* satellite, the far-UV absorption bands of H_2 have been observed in the Galactic disk toward numerous relatively bright stars with visual extinctions A_{V} of less than about 1 mag (e.g. Spitzer & Jenkins 1975; Savage et al. 1977). More recent observations of H_2 with the *Interstellar Medium Absorption Profile Spectrograph* (IMAPS) (Jenkins & Peimbert 1997), the *Orbiting and Retrievable Far and Extreme Ultraviolet Spectrometer* (ORFEUS) (Richter et al. 1998; de Boer et al. 1998), and the *Far Ultraviolet Spectroscopic Explorer* (FUSE) (Moos et al. 2000) have shown the ubiquity of H_2 in the disk and halo of the Galaxy and in the Magellanic Clouds. In the FUSE mini-survey, H_2 was detected in the sightlines with neutral hydrogen column densities

$N(\text{H I}) \simeq (3 \div 6) \times 10^{20} \text{ cm}^{-2}$, the fractional abundances $f_{\text{H}_2} \simeq 7.4 \times 10^{-6} \div 3.4 \times 10^{-2}$ and the excitation temperatures $T_{\text{ex}} \simeq 180 \div 540$ K (Shull et al. 2000).

In these observations the range of $N(\text{H I})$ resembles the range of hydrogen column densities measured in QSO damped Ly α systems (DLA hereinafter) – the systems with $N(\text{H I}) > 2 \times 10^{20} \text{ cm}^{-2}$, which are believed to originate in intervening galaxies or proto-galaxies located at cosmological distances (Wolfe et al. 1995). Thus we may expect to observe far-UV H_2 lines from electronic-vibrational-rotational bands shifted to the blue spectral range ($\lambda > 3000 \text{ \AA}$) at $z \gtrsim 2$. The detection of the first H_2 -bearing cosmological cloud in the $z_{\text{abs}} = 2.811$ DLA system toward Q0528–250 was made by Levshakov & Varshalovich (1985) and later confirmed by Foltz, Chaffee, & Black (1988). Two additional H_2 systems were found at $z_{\text{abs}} = 1.97$ toward Q0013–004 (Ge & Bechtold 1997) and at $z_{\text{abs}} = 2.34$ toward Q1232+0815 (Ge & Bechtold 1999). The latter was recently confirmed by Petitjean, Srianand, & Ledoux (2000). The fourth identification of H_2 was made at $z_{\text{abs}} = 3.39$ toward Q0000–2620 by Levshakov et al. (2000b, 2001) and a tentative fifth H_2 system was reported by Petitjean et al. (2000) at $z_{\text{abs}} = 2.374$ toward Q0841+129.

Molecular gas in the early Universe has also been detected through the spectral-line emission from the tracer carbon monoxide (CO) molecule in the ultraluminous galaxy IRAS 10215+4724 at $z = 2.28$ (Brown & Van den Bout 1992; Solomon, Downes, & Radford 1992), in the clover-leaf quasar H1413+117 at $z = 2.56$ (Barvainis et al. 1997), in the quasar BR1202–0725 at $z = 4.69$ (Ohta et al. 1996; Omont et al. 1996), in the quasar BRI1335–0418 at $z = 4.41$ (Guilloteau et al. 1997; Carilli, Menten, & Yun 1999), in the IR luminous galaxy J14011+0252 at $z = 2.565$ (Frayser et al. 1999), in the extremely red galaxy HR10 at $z = 1.44$ (Andreani et al. 2000), in two powerful radio galaxies 4C60.07 and 6C1909+722 at $z = 3.79$ and 3.53, respectively (Papadopoulos et al. 2000), in the lensed quasar APM08279+5255 at $z = 3.911$ (Downes et al. 1999; Papadopoulos et al. 2001) and in the QSO SDSS 1044–0125 at $z = 5.8$ (Iwata et al. 2001).

However, identification of H_2 lines in the damped Ly α systems remains a rather rare

¹Based on public data released from UVES Commissioning at the VLT Kueyen telescope, ESO, Paranal, Chile.

²Division of Theoretical Astrophysics, National Astronomical Observatory, Tokyo 181-8588, Japan; lev@th.nao.ac.jp.

³Department of Theoretical Astrophysics, Ioffe Physico-Technical Institute, St. Petersburg 194021, Russia; lev@astro.ioffe.rssi.ru.

⁴European Southern Observatory, Karl-Schwarzschild-Str. 2, D-85748 Garching bei München, Germany; sdodoric@eso.org.

⁵Observatoire de Genève, CH–1290 Sauverny, Switzerland; mdessaug@eso.org.

⁶Osservatorio Astronomico di Trieste, Via G.B. Tiepolo 11, I-34131 Trieste, Italy; molaro@oat.ts.astro.it.

event. Most DLAs yielded only upper limits of $f_{\text{H}_2} \lesssim 10^{-7} \div 10^{-6}$. The lack of H_2 in these systems might be a consequence of the lower metal abundances, lower dust contents, higher temperature and ultraviolet fluxes when compared with the ISM in the Galaxy and in the Magellanic Clouds. Low molecular abundances found in high redshift DLAs resemble the properties of, at least, one local DLA system – the metal-deficient ($Z/Z_\odot \sim 1/50$) starburst blue compact galaxy I Zw 18 with $N(\text{H I}) \simeq 3 \times 10^{21} \text{ cm}^{-2}$ (Kunth et al. 1994) where recent FUSE observations set a limit of $f_{\text{H}_2} \ll 10^{-6}$ (Vidal-Madjar et al. 2000).

The measured upper limits of f_{H_2} in high redshift metal-poor DLAs are slightly lower than the calculated fraction of molecules in the pristine gas – $f_{\text{H}_2} \simeq 10^{-6} \div 10^{-5}$ depending on cosmological models (e.g. Galli & Palla 1998). Although UV photons produced by the first objects can quickly destroy all H_2 in the pristine gas and thus delay further structure formation (Haiman, Rees, & Loeb 1997), we may expect that the electrons in the photoionized regions around first stars will in turn act as a catalyst in the H^- channel to produce H_2 at redshifts $z < 50$ where the H^- channel proceeds much more quickly than the H^+ one (Fuller & Couchman 2000). Therefore direct measurements of gas density, UV radiation field, and H_2 formation and destruction rates in DLA systems may shed light on star formation processes at very high redshift.

In this paper we present results of the study of H_2 lines identified in the sixth DLA system at $z_{\text{abs}} = 3.025$ toward Q0347–3819. We also use the information from the molecular lines together with H and metal lines to refine the deuterium abundance determination by D’Odorico, Dessauges-Zavadsky, & Molaro (2001, hereinafter DDM) and the values of metal abundances (DDM; Prochaska & Wolfe 1999).

The outline of the paper is as follows. We discuss observations in Section 2. The methods of data analysis are presented in Section 3. The identification of H_2 lines and the calculation of their proper redshift is given in § 3.1. The broadening b -parameter is evaluated in § 3.2. The column densities $N(J)$ for the rotational levels from $J = 0$ to 5 of the lowest vibrational level $v = 0$ in the ground electronic state $X^1\Sigma_g^+$ (for the H_2 notation, see

Field et al. 1966), the fractional molecular abundance, and the ortho:para- H_2 ratios are calculated in § 3.3. In § 3.4 we compute the excitation temperature T_{ex} . The results of a stacking technique applied to the measurements of the abundances of Zn II and Cr II ions and the dust-to-gas ratio in the whole $z_{\text{abs}} = 3.025$ system are estimated in § 3.5. In § 3.6 we analyze within one self-consistent model all available profiles of H, D, neutral atoms and low ions to infer column densities and relative abundances of D/H and metals. In Section 4 we discuss the results and present their further analysis. In § 4.1 we estimate the kinetic temperature, T_{kin} , and the gas volumetric density, n_{H} , using the C II*/C II and C I/C II ratios. The distribution of H_2 over the rotational levels, the photodissociation rate of H_2 and the rate of the molecular hydrogen formation upon grain surfaces are considered in § 4.2. The revealed [α -element/iron-peak] enhancement is discussed in § 4.3. In Section 5 we summarize the results.

2. Observations

Q0347–3819 is a bright quasar ($V = 17.3$) with $z_{\text{em}} = 3.23$ discovered by Osmer & Smith (1980), which shows a damped Ly α system at $z_{\text{abs}} = 3.0245$. A column density of $N(\text{H I}) = (6.3_{-1.3}^{+1.6}) \times 10^{20} \text{ cm}^{-2}$ was first measured by Williger et al. (1989) and later confirmed by Pettini et al. (1994) as $N(\text{H I}) = (5 \pm 1) \times 10^{20} \text{ cm}^{-2}$. Q0347–3919 has a rich absorption-line spectrum studied by Pierre, Shaver, & Robertson (1990), Centurión et al. (1998), Ledoux et al. (1998), and by Prochaska & Wolfe (1999).

High-quality data of this QSO in the UV ($3650 \text{ \AA} < \lambda < 4900 \text{ \AA}$) and in the near-IR ($6700 \text{ \AA} < \lambda < 10000 \text{ \AA}$) ranges were obtained during the commissioning of the UVES on the VLT 8.2m Kueyen telescope at Paranal, Chile, in December 1999, and have been released for public use. The UVES spectrograph is described by D’Odorico et al. (2000) and details of the data reduction are given in Ballester et al. (2000). Two exposures of 4500 s and 5000 s, covering the UV and the near-IR ranges, were obtained with a resolution $\text{FWHM} \simeq 7.0 \text{ km s}^{-1}$ and $\simeq 5.7 \text{ km s}^{-1}$, respectively. An average signal-to-noise ratio per pixel of $\sim 20, 25, 40$ and 15 was achieved in the final spectrum at $\lambda \sim 3650 \text{ \AA}$, 4900 \AA , 6700 \AA , and

10000 Å, respectively.

The $z_{\text{abs}} = 3.025$ DLA exhibits a multicomponent velocity structure with the dominating component at $z_{\text{abs}} = 3.024856$ as found by DDM who discussed the first detection of the deuterium lines in DLAs. The total H I column density derived in DDM from the best fit of Ly β equals $(4.3 \pm 1.0) \times 10^{20} \text{ cm}^{-2}$, which agrees well with the measurement of Pettini et al. (1994) from Ly α . The ionization structure of this DLA is also complex. There are at least two gas components: a warm gas seen in lines of neutral atoms, H₂, and low ions, and a hot gas where the resonance doublets of C IV and Si IV are formed. These high-ion transitions, observed by Prochaska & Wolfe (1999) with the Keck HIRES spectrograph show, however, different profile shapes as compared with the low ion-transitions. The physical properties of the hot gas component will not be studied in the present paper.

3. Measurements

All absorption lines studied in the present paper lie in the Ly α forest where their analysis is complicated by possible H I contaminations and uncertainties in a local continuum, drawn by using ‘continuum windows’ in the Ly α forest which could be located quite far from the feature under analysis. This kind of uncertainties is illustrated in Figure 1 where a portion of the Q0347–3819 spectrum with a few identified H₂ lines is shown. To achieve the highest possible accuracy under these circumstances, we have always used in parallel several different lines to derive the physical parameters of the DLA system.

3.1. Redshift of the H₂ system

Wavelengths, oscillator strengths, and radiation damping constants for the Lyman and Werner bands of the H₂ molecule were taken from the theoretical calculations of Abgrall & Roueff (1989). These data seem to be reasonably accurate as shown by high spectral resolution IMAPS measurements of molecular hydrogen toward the Orion belt stars (Jenkins et al. 2000).

The identification of the H₂ lines was started from the subsystem which has the largest H I column density (see § 3.6). Preliminary inspection of the Q0347–3819 spectrum revealed 88 absorption

features at the expected positions of the H₂ lines. However, not all of them were suitable for further analysis due to H I contaminations. For this reason, to estimate z_{H_2} we used only those H₂ lines which show symmetric profiles with their blue and red sides reaching the continuum. These lines are listed in Table 1 (see also Figures 5 and 6).

Given a fit to the continuum and the line measurement interval, the equivalent width W_λ , the line center $\langle \lambda \rangle$ and their errors σ_{W_λ} and $\sigma_{\langle \lambda \rangle}$ can be computed from the following equations (e.g. Levshakov et al. 1992):

$$W_\lambda = \Delta\lambda \sum_{i=1}^M (1 - F_i), \quad (1)$$

$$\langle \lambda \rangle = \frac{\Delta\lambda}{W_\lambda} \sum_{i=1}^M \lambda_i (1 - F_i), \quad (2)$$

$$\sigma_{W_\lambda} = \Delta\lambda \left[\sum_{i=1}^M \sigma_i^2 + \left\langle \frac{\sigma_c}{C} \right\rangle^2 (M - W')^2 \right]^{1/2}, \quad (3)$$

and

$$\sigma_{\langle \lambda \rangle} = \left[\frac{\Delta\lambda}{W_\lambda} \sum_{i=1}^M (\lambda_i - \langle \lambda \rangle)^2 (1 - F_i) \right]^{1/2}, \quad (4)$$

where $\Delta\lambda$ is the wavelength interval between pixels, M is the number of pixels involved in the sum, F_i is the normalized intensity in the i th pixel whose wavelength is λ_i , σ_i is the noise level in the i th pixel, $W' = W_\lambda/\Delta\lambda$ is the dimensionless equivalent width in pixels, and $\langle \sigma_c/C \rangle$ is the mean accuracy of the continuum fit over the line measurement interval.

The errors in W_λ and $\langle \lambda \rangle$ are caused mainly by the finite number of photons counted. In addition, for weak absorption features ($W' \ll 1$) the second term in equation (3) is of about the same order of magnitude as the first one, meaning that the identification of weak H₂ lines is very sensitive to the accuracy of the local continuum fitting.

The analyzed 35 transitions of the Lyman and Werner bands are listed in column (2) of Table 1, whereas their J-values are given in column (1). The measured heliocentric position of the center of each spectral feature and its standard deviation were calculated according to equations (2) and (4) and are presented in columns

(3) and (4), respectively. The observed equivalent widths (column 5) and their errors (column 6) were calculated according to equations (1) and (3). Note that the rest frame equivalent width equals $W_{\lambda, \text{rest}} = W_{\lambda} / (1 + z_{\text{H}_2})$. In these calculations we set for all lines $\langle \sigma_c / C \rangle = 1\%$ to account for the uncertainty in the local continuum level. A formal mean value of $\langle \sigma_c / C \rangle$ estimated from the continuum windows is less than or about 1%. In particular, $\langle \sigma_c / C \rangle = 0.70\%$ for L3-0R(0) and 1.03% for L7-0P(5) which are shown in Figures 5 and 6, respectively. Column (7) lists the measured redshifts for each H₂ transition, their errors $|\sigma_z| = |\sigma_{(\lambda)}| / \lambda_0$ (where λ_0 is the rest frame wavelength from Abgrall & Roueff 1989) are shown in column (8). The weighted mean redshift yields $z_{\text{H}_2} = 3.024855 \pm 0.000005$, which coincides exactly with the redshift of the strongest main component in metal line profiles given by DDM. Thus, at a given S/N ratio and spectral resolution we do not find any systematic shifts larger than a few km s⁻¹ in the radial velocities between neutral atoms and H₂ molecules in the molecular cloud at $z_{\text{abs}} = 3.025$.

Previous *Copernicus* investigations of diffuse gas in the Galaxy showed that the mean radial velocity of H₂ lines differs from the corresponding mean of the atomic lines. For instance, the differences of $\Delta v \simeq 5$ km s⁻¹ toward λ Sco (Spitzer & Jenkins 1975), $\Delta v \simeq 11$ km s⁻¹ and $\simeq 6$ km s⁻¹ toward, respectively, τ Sco and ζ Oph (Spitzer, Cochran, & Hirshfeld 1974) were detected. At the UVES spectral resolution such differences – in case they were present – could be easily distinguished.

3.2. Line broadening

The measurement of the broadening b^7 parameter and the calculation of the confidence ranges for its mean value were carried out in two steps.

First, a least-squares analysis was applied to the line fitting. We combined 17 H₂ lines (L3-0R0, L7-0R0, W3-0Q1, L3-0P1, W0-0R2, W0-0Q2, L3-0R2, L4-0R2, L2-0P3, L2-0R3, L4-0R3, L4-0P3, L8-0P3, L12-0R3, L4-0P4, L8-0P4, W1-0Q5) from Table 1 and fitted them simultaneously with the

⁷ By definition $b = \sqrt{2} \sigma_v$, where σ_v is the one-dimensional Gaussian velocity dispersion of molecules along the line of sight.

individual Gaussian profiles. These lines were chosen because they exhibit ‘clean’, uncontaminated profiles. The H₂ line centers were fixed at the mean z_{H_2} and the theoretical profiles were convolved with the instrumental point-spread function (PSF) which was approximated by a Gaussian with FWHM = 7.0 km s⁻¹, i.e. $b_{\text{PSF}} = 4.2$ km s⁻¹. The $\Delta\chi^2$ method (Press et al. 1992) was used to estimate the most probable b value and its error⁸. For a given current value of b taken from the range $[b_{\text{min}}, b_{\text{max}}]$, we minimized χ^2 (normalized per degree of freedom) by varying the line intensities independently (we consider χ_{min}^2 as a χ^2 distribution with $\nu = \mathcal{N} - \mathcal{M}$ degrees of freedom, where the number of data points $\mathcal{N} = 192$ and the number of fitted parameters $\mathcal{M} = 6$ for this particular case). With this we tried to check possible H I contaminations: the optimization procedure would fail to reach $\chi_{\text{min}}^2 \simeq 1$ if the chosen H₂ lines were essentially contaminated by the Ly α forest absorption. The calculated χ_{min}^2 values in dependence of b and the 1 σ and 2 σ confidence levels are shown in Figure 2. With $\chi_{\text{min}}^2 = 0.925$ the most likely value for b_{H_2} was found to be 2.80 ± 0.45 km s⁻¹ (s.d.).

In the second step, to check the obtained value and to infer the Doppler parameter independently, we calculated an optimal curve of growth for the H₂ lines from Table 1. The curve is shown by the solid line in Figure 3. In principle, it cannot be excluded that some unknown absorption lines blend with H₂ features, despite their symmetric and undisturbed profiles. Thus, the scatter of points in Figure 3 can be explained by this effect as well as by errors remaining after the continuum fitting. It is also seen from Figure 3 that the strongest absorption lines from J = 1 and 3 levels are slightly saturated and therefore their equivalent widths are sensitive to the assumed broadening model. The data for these levels give the effective Doppler width $b \simeq 3$ km s⁻¹. We also depicted two curves for $b = 2$ km s⁻¹ and 4 km s⁻¹ to demonstrate the complete consistency of b -values estimated in both approaches.

⁸ In the present paper, the estimated standard errors are slightly larger than those calculated by the Monte Carlo method because the pipeline resampling to constant wavelength bins introduces a correlation between data point values, whereas the estimated mean values of the physical parameters remain unbiased (see Appendix A).

We note that Jenkins & Peimbert (1997) have measured an interesting phenomenon of increasing b -values for H_2 lines arising from progressively higher rotational levels in a spectrum of ζ Ori A. The most probable Doppler parameters were found to be : $b(0) = 0.8 \text{ km s}^{-1}$, $b(1) = 2.7 \text{ km s}^{-1}$, $b(2) = 5.3 \text{ km s}^{-1}$, $b(3) = 5.9 \text{ km s}^{-1}$, and $b(5) = 9.0 \text{ km s}^{-1}$. As they noted, such profile shapes are inconsistent with a simple model of UV optical pumping which governs the H_2 rotational populations in an optically thin, homogeneous medium. They suggested that these H_2 profiles with changing shapes ‘may represent molecules forming in the postshock gas that is undergoing further compression as it recombines and cools’. A similar phenomenon may also be observed in high redshift DLAs which can be associated to star forming regions where shocks are very probable.

The $z_{\text{abs}} = 3.025$ system presents the weakest members of the Lyman and Werner series with $J = 4$ and 5 but, unfortunately, we are unable to compare their b -values with those from lower rotational transitions because our signal-to-noise ratio is not sufficiently high. Thus, in the following we assume a simple one-component model for the molecular cloud with a common broadening parameter $b_{\text{H}_2} = 2.80 \text{ km s}^{-1}$ for all molecular hydrogen lines.

3.3. H_2 abundances

In the final fitting of each line profile we combined together the H_2 lines with the same J to yield the corresponding $N(J)$ column densities and their confidence regions. A χ^2 minimization procedure was applied simultaneously to all lines from a given rotational level J . To control solutions at this stage, we added to the lines listed in Table 1 a few weaker transitions where we observe continuum without any pronounced absorption features at their expected positions. The calculated χ_{min}^2 values and the 1σ and 2σ confidence levels for each individual rotational level J are shown in Figure 4. The curves $\chi^2[N(J)]$ were computed with the fixed mean $b_{\text{H}_2} = 2.80 \text{ km s}^{-1}$ and the mean z_{H_2} . The H_2 lines involved in the analysis are as follows: L3-0R0, and L7-0R0 ($\mathcal{N} = 22$); L3-0P1, and L14-0P1 ($\mathcal{N} = 20$); W0-0R2, W0-0Q2, L3-0R2, L4-0R2, and L5-0R2 ($\mathcal{N} = 51$); W2-0R3, L2-0R3, L2-0P3, L3-0R3, L3-0P3, L4-0R3, L6-0R3, L7-0P3, L8-0P3, L12-0R3, and L15-0R3

($\mathcal{N} = 83$); L5-0R4, L6-0R4, and L8-0P4 ($\mathcal{N} = 34$); L7-0P5, and L12-0R5 ($\mathcal{N} = 21$). The most probable column densities and their errors at the 1σ confidence level are: $N(0) = (1.90 \pm 0.35) \times 10^{13} \text{ cm}^{-2}$, $N(1) = (1.60 \pm 0.18) \times 10^{14} \text{ cm}^{-2}$, $N(2) = (5.40 \pm 0.35) \times 10^{13} \text{ cm}^{-2}$, $N(3) = (1.22 \pm 0.05) \times 10^{14} \text{ cm}^{-2}$, $N(4) = (2.60 \pm 0.43) \times 10^{13} \text{ cm}^{-2}$, and $N(5) = (2.90 \pm 0.70) \times 10^{13} \text{ cm}^{-2}$. From that we calculate the total column density in H_2 , $N(\text{H}_2) = \sum_J N(J) = (4.10 \pm 0.21) \times 10^{14} \text{ cm}^{-2}$, and the ratio of the total column densities in the ortho- and para- H_2 states $N_{\text{ortho}}/N_{\text{para}} = 3.1 \pm 0.3$ (s.d.). This result can be compared with two other molecular clouds at $z_{\text{abs}} = 2.8112$ (Q0528-250, Srianand & Petitjean 1998) and $z_{\text{abs}} = 2.33771$ (Q1232+0815, Srianand et al. 2001) where $N(J)$ values were also measured for different J . Using the published $N(J)$ values and their errors, we found $N_{\text{ortho}}/N_{\text{para}} = 3.1 \pm 0.8$ (s.d.) at $z_{\text{abs}} = 2.8112$ and $N_{\text{ortho}}/N_{\text{para}} = 2.4 \pm 0.9$ (s.d.) at $z_{\text{abs}} = 2.33771$.

According to our calculations presented in Section 3.6, the total H I column density in the $z_{\text{abs}} = 3.025$ system is $(4.225 \pm 0.045) \times 10^{20} \text{ cm}^{-2}$. With $N(\text{H}_2) = (4.10 \pm 0.21) \times 10^{14} \text{ cm}^{-2}$, the ratio of H nuclei in molecules to the total H nuclei is

$$f_{\text{H}_2} = \frac{2 N(\text{H}_2)}{N(\text{H})} = (1.94 \pm 0.10) \times 10^{-6}.$$

To test the consistency of the estimated physical parameters with the observed absorption features, we calculated theoretical profiles for all 88 H_2 lines using the derived mean z_{H_2} , b_{H_2} , and $N(J)$ values. Besides we calculated 8 profiles for H_2 transitions where no absorption features have been observed at the continuum level. The latter are L3-0R4, L9-0R4, L4-0R5, L9-0R5, L11-0P5, W0-0Q5, L6-0P6, and L7-0R7. The last two of them give upper limits to $N(6) < 2.0 \times 10^{13} \text{ cm}^{-2}$ (1σ c.l.), and to $N(7) < 8.0 \times 10^{12} \text{ cm}^{-2}$ (1σ c.l.).

The observational and over-plotted theoretical H_2 profiles are shown in Figures 5 and 6. In these figures possible blends with other lines from the $z_{\text{abs}} = 3.025$ DLA and from the metal systems listed in Appendix B are also indicated. We found only one large inconsistency between observable and theoretical profiles, namely for the W2-0Q(3) line (Figure 6). But in this case a very wide absorption trough between 3901 \AA and 3921 \AA redward the redshifted position of this molecular

line ($\lambda_{\text{obs}} = 3900.3 \text{ \AA}$) prevents the accurate estimation of the local continuum level. Uncertainties in the local continuum level calculations may also cause over-absorption in the synthetic profiles as compared with the observable profiles seen in W1-0R0+R1, W2-0Q1 (Figure 5), W0-0Q3, L3-0P3, L4-0P3, L10-0R3, L12-0R3, W0-0Q5, and L4-0R5 (Figure 6). In all other cases the synthetic H_2 profiles are in agreement with the absorption-line features identified with the H_2 lines in the UV spectrum of Q0347–3819.

We have also tried to detect the H_2 molecules in the blue component at $\Delta v \simeq -17 \text{ km s}^{-1}$ (see § 3.6) with respect to the main H_2 -bearing component but we found only an upper limit. The applied method is similar to that employed by Levshakov et al. (1989) to improve the detectability of weak carbon monoxide (CO) UV lines in damped Ly α systems.

The procedure consists of shifting the observed spectral regions containing expected positions of the H_2 transitions, which are not contaminated by the apparent Ly α forest absorption, into the relative velocity scale centered at $z = 3.024637$, – the redshift of the blue subcomponent of the dominant metal absorption in the $z_{\text{abs}} = 3.025$ DLA, and of the consequent stacking of these regions. Before co-adding each section, the data are rebinned with a bin size of 1.45 km s^{-1} . The spectra were then averaged with weights in accord with the squares of the expected relative line strengths divided by the respective signal-to-noise ratios.

The result obtained from this stacking procedure is shown in Figure 7. The composite spectrum formed by the addition of 18 H_2 bands (with no pronounced absorption features in the range $\Delta v = \pm 6 \text{ km s}^{-1}$) which are labeled in the corresponding panels is depicted in the bottom panel. The resulting co-added data have an average S/N $\simeq 100$ and show no absorption at $v = 0 \text{ km s}^{-1}$, whereas the blue wing of the composed molecular line from the $z = 3.024855$ system is clearly seen at $v \simeq +16 \text{ km s}^{-1}$.

The composite spectrum gives $W_{\lambda, \text{rest}} < 0.6 \text{ m\AA}$ (3σ c.l.) for the equivalent width of the sum of the H_2 bands in the rest frame of the absorber. This limit is sensitive, in general, to errors in continuum fitting. In our case the resulting profile between $-6 \text{ km s}^{-1} < v < 6 \text{ km s}^{-1}$ has no apparent deviations from unity, the estimated mean value

is $\langle C \rangle = 1.003 \pm 0.003$ and thus $\langle \sigma_c / C \rangle = 0.003$. Substituting these values in equation (3) we obtain the limiting equivalent width ($W' \ll 1$) $\sigma_{\text{lim}} = 0.2 \text{ m\AA}$ and $W_{\lambda, \text{rest}} = 0.6 \text{ m\AA}$ ($3\sigma_{\text{lim}}$).

For a weak absorption line with the central optical depth $\tau_0 \ll 1$, the column density is independent of the broadening parameter b and is linearly proportional to the equivalent width W_λ :

$$N = 1.13 \times 10^{20} \frac{W_\lambda}{\lambda_0^2 f}, \text{ cm}^{-2} \quad (5)$$

where f is the oscillator strength for the absorption transition, λ_0 is the line center rest wavelength in \AA , and W_λ is the rest equivalent width in \AA .

Using this linear approximation to the curve of growth, we calculate the composite equivalent width W_J for the H_2 bands from the same J level

$$W_J = a N_J \sum_i \lambda_{J,i}^2 f_{J,i}, \quad (6)$$

where $a = 8.85 \times 10^{-21}$.

Then the total equivalent width for all H_2 bands presented in Figure 7 is

$$W_\Sigma = \sum_J W_J = a \sum_J \epsilon_J N_J = a \hat{\epsilon} N_{\text{H}_2}, \quad (7)$$

where $\epsilon_J = \sum_i \lambda_{J,i}^2 f_{J,i}$, $\hat{\epsilon}$ is an effective value (in our estimation $\hat{\epsilon} = \max \epsilon_J$), and $N_{\text{H}_2} = \sum_J N_J$.

The coefficients ϵ_J do not vary significantly and for the H_2 bands from Figure 7 $\epsilon_0 = 6.1 \times 10^4$, $\epsilon_1 = 5.5 \times 10^4$, $\epsilon_2 = 5.3 \times 10^4$, and $\epsilon_3 = 9.8 \times 10^4$. Thus, the aforementioned upper limit $W_\lambda < 0.6 \text{ m\AA}$ and equation (7) yield $N(\text{H}_2) < 7.0 \times 10^{11} \text{ cm}^{-2}$ (3σ c.l.) and $f_{\text{H}_2} < 3.3 \times 10^{-9}$ (3σ c.l.), which is well below that found in Galactic H I clouds. It means that molecular hydrogen is not homogeneously distributed in the $z_{\text{abs}} = 3.025$ absorbing region.

The measured $N_{\text{ortho}}/N_{\text{para}}$ ratios in the DLAs at $z_{\text{abs}} = 3.025$ (Q0347–3819), 2.8112 (Q0528–250), and 2.33771 (Q1232+0815) are equal to 3 (within the uncertainty interval), which is just the equilibrium value for the ortho:para ratio at the hot formation of H_2 on grain surfaces in relatively transparent clouds (e.g., Spitzer & Morton 1976). In the pristine gas, the ortho:para H_2 ratio decreases from the equilibrium value of

3 at $z \simeq 100$ to its ‘freeze-out’ quantity of 0.25 at $z < 20$ (Flower & Pineau des Forêts 2000). Thus, we can conclude that H_2 observed in these DLAs has undergone a re-forming phase following photo-dissociation of the pristine H_2 .

3.4. Excitation temperature

In the ground electronic-vibrational state, all the rotational levels with odd J are nuclear triplet states (ortho- H_2), and all those with the even J are singlet states (para- H_2). Thus, for the ortho- H_2 the statistical weight, $g(J)$, of a level J equals $3(2J+1)$, whereas for the para-molecules $g(J) = (2J+1)$. In thermal equilibrium, the collisionally dominated distribution of molecules over different J levels is given by a Boltzmann law with an effective excitation temperature T_{ex}

$$\frac{N(J)}{N(0)} = \frac{g(J)}{g(0)} \exp \left[-\frac{B_v J(J+1)}{T_{\text{ex}}} \right], \quad (8)$$

where the constant B_v equals 85.36 K for the vibrational ground state.

This equation shows that T_{ex} is proportional to the negative inverse of the slope of a line (called ‘the excitation diagram’) drawn through the points of the respective J levels in a plot $\log [N(J)/g(J)]$ versus $E(J)$, where $N(J)$ is the column density measured in the rotational level J , $E(J)$ is the excitation energy of this level relative to $J = 0$, and $g(J)$ is its statistical weight. Figure 8 shows this diagram for different J levels. A least-squares fit, weighted by $1/\sigma^2$ for each $\log [N(J)/g(J)]$, yields $T_{\text{ex}} = 825 \pm 110$ K (s.d.) and $\log N(0) = 13.31 \pm 0.03$ in cm^{-2} (s.d.). This value of $N(0)$ agrees well with what has been measured from profile fitting in § 3.3. Thus, we find that the population of the six lowest J levels can be fitted with a single Boltzmann distribution.

The unique T_{ex} for all levels from $J = 0$ to 5 may imply that the H_2 rotational population is dominated by collisions in a gas whose kinetic temperature is about 800 K. The kinetic temperature in the H_2 cloud can be estimated from the widths of the H_2 and metal lines. In § 3.6, we show that profiles of all metals from C II to Zn II can be described with the same broadening parameter of $b_{\text{Me}} = 2.71 \pm 0.05$ km s^{-1} . With $b_{\text{H}_2} = 2.80 \pm 0.45$ km s^{-1} , it gives an upper limit of $T_{\text{kin}} \leq 430$ K in the main H_2 -bearing component. The fact that

T_{kin} is less than T_{ex} indicates that the population of the low J levels is caused not only by collisions but by UV-pumping as well. The $J = 0$ and 1 rotational levels, being usually populated in dense molecular clouds by thermal proton collisions, may not be in equilibrium with the kinetic temperature in lower density clouds which are not optically thick in the L0-0R(0), R(1), P(1) and W0-0R(0), R(1), Q(1) lines. In low density clouds the self-shielding effects are negligible and do not reduce significantly UV-pumping in these lines (e.g., Shull & Beckwith 1982). For the further analysis we set $T_{\text{kin}} = 400$ K to be consistent with the measured b -values.

3.5. Cr/Zn and dust content

Copernicus H_2 survey has shown that in our Galaxy the molecular fraction f_{H_2} is correlated with $E(B-V)$ and with the total neutral hydrogen column density (e.g. Spitzer & Jenkins 1975). The presence of dust grains in damped $\text{Ly}\alpha$ systems is usually estimated from the abundance ratio $[\text{Cr}/\text{Zn}]^9$ assuming that Zn is undepleted (Petitini et al. 1994).

Preliminary visual inspection of the red part of the Q0347–3819 spectrum has shown weak absorption features at the expected positions of Zn II and Cr II lines. In order to increase sensitivity and to measure the abundance ratio $[\text{Cr}/\text{Zn}]$ we applied a stacking procedure similar to the one described in § 3.3 to the Zn II $\lambda 2026.136$ Å and $\lambda 2062.664$ Å lines, and to the Cr II $\lambda 2056.254$, Å $\lambda 2062.234$, Å and $\lambda 2066.161$ Å lines. The wavelengths and the oscillator strengths for these lines are taken from Morton (1991), and from Bergeson & Lawler (1993), respectively. The resulting composite spectra of Zn II and Cr II were included in the metal analysis in the next § 3.6 (see Figure 10 and Tables 3 and 4). In this Figure, two pronounced absorption features at $\Delta v \simeq +6$ km s^{-1} (Cr II) and at $\Delta v \simeq +13$ km s^{-1} (Zn II) are telluric lines. The former partly blends the red wing of the Cr II line, therefore we do not use this portion of the Cr II profile in the fitting procedure. The estimated total column densities are

⁹ $[\text{X}/\text{Y}] = (\text{X}/\text{Y}) - (\text{X}/\text{Y})_{\odot}$, where (X/Y) is the logarithmic value of the element ratio by number without reference to the solar value. Solar abundances $(\text{X}/\text{Y})_{\odot}$ are taken from Grevesse & Sauval (1998).

$N(\text{Zn II}) = (6.19 \pm 0.51) \times 10^{11} \text{ cm}^{-2}$, and $N(\text{Cr II}) = (2.76 \pm 0.22) \times 10^{12} \text{ cm}^{-2}$. With these numbers one finds $[\text{Cr}/\text{Zn}] = -0.37 \pm 0.06$.

In Table 2 we summarize the results of the abundance measurements of molecular hydrogen, $[\text{Cr}/\text{Zn}]$ (and/or $[\text{Fe}/\text{Zn}]$), and neutral hydrogen in the DLAs available up to now. The presence of dust in these DLAs and the relation between the fractional molecular abundances and relative heavy element depletion is illustrated in Figure 9. The measured data for the five extragalactic molecular clouds (marked by numbers in Figure 9) can be fitted with a linear law : $\log f_{\text{H}_2} = A [\text{Cr}/\text{Zn}] + B$, with $A = -6.053 \pm 0.116$ and $B = -7.888 \pm 0.051$. The linear regression is shown in Figure 9 by the solid line¹⁰. Again, similarly to our previously obtained results (Levshakov et al. 2000b), we find a strong correlation between $\log f_{\text{H}_2}$ in the DLA systems with detectable H_2 absorption and the heavy element depletion. The presence of upper limits below the linear regression line may be explained by the suggestion that in these systems a relatively high temperature of dust grains prevents molecular formation.

The degree of the heavy element depletion may be used to estimate the dust-to-gas ratio, \tilde{k} , if two measured elements have the same nucleosynthesis history (cf. Vladilo 1998) :

$$\tilde{k} = \frac{10^{[\text{Zn}/\text{H}]_{\text{obs}}}}{f_{\text{Zn,ISM}} - f_{\text{Cr,ISM}}} \left(10^{[\text{Cr}/\text{Zn}]_{\text{obs}}} - 1 \right), \quad (9)$$

where the fraction in dust $f_{\text{Zn,ISM}} = 0.35$ and $f_{\text{Cr,ISM}} = 0.92$ refers to the Galactic interstellar medium.

Error propagation method applied to the column density measurements yields $[\text{Zn}/\text{H}] = -1.503 \pm 0.054$, and then Eq. (9) results in the average value for the whole DLA $\tilde{k}_{\text{DLA}} = 0.032 \pm 0.005$ (1σ c.l.) showing that the dust content in the $z_{\text{abs}} = 3.025$ absorber is approximately

30 times lower as compared with the Milky Way. If, however, we consider the same quantity for the H_2 -bearing cloud using the data from Table 3, then $\tilde{k} \simeq 0.047$, i.e. the dust content in the molecular cloud is about 1.5 times higher as compared with the average value.

3.6. D/H and metal abundances

In this section we study metal profiles and derive a new D/H ratio by fitting simultaneously the available Lyman series lines and metals. The knowledge of the proper distribution of the velocity components along the line of sight is especially crucial for the D/H measurements, since D I lines are always blended with the blue wings of the corresponding H I lines (for numerous examples, see Levshakov, Kegel, & Takahara 1999 and references cited therein).

In the UVES spectrum of Q 0347–3819, at $z_{\text{abs}} = 3.025$ we have identified absorption lines of C II, N I, O I, Si II, P II, Ar I, Cr II, Fe II, Zn II, and C II*. The identified metal absorption lines are shown in Figure 10, and in Figure 11 – the atomic hydrogen lines. The atomic data were taken mainly from Morton (1991) with a few additions of new results for Si II from Spitzer & Fitzpatrick (1993) and Charro & Martín (2000), for Ar I from Federman et al. (1992), for Cr II and Zn II from Bergeson & Lawler (1993), for Fe II from Cardelli & Savage (1995), Raassen & Uylings (1998), and Howk et al. (2000).

To construct a model for the radial velocity distribution, we firstly analyzed the profiles of each individual atom/ion to select lines (or parts of them) which are less contaminated and disturbed by the $\text{Ly}\alpha$ forest absorption. The chosen profiles and/or their components are marked in Figures 10 and 11 by horizontal lines at the bottoms of the panels (these horizontal lines also show the pixels involved in the final optimization procedure). Other spectra in Figures 10 and 11, not marked by the horizontal lines, were used to control consistency of the obtained results.

Our model is based on the following assumptions: (i) the whole DLA is considered as a continuous absorbing region with fluctuating gas density and velocity fields. (ii) The metallicity for each element is set constant through the DLA. (iii) Some of the observed species may have similar profiles,

¹⁰ For the published 27 DLAs where all three elements Zn II, Cr II, and Fe II were measured, $[\text{Cr}/\text{Fe}] = 0.12 \pm 0.13$ (s.d.). This implies that Fe is slightly more depleted than Cr assuming both elements track each other in the abundances and, thus, the slope in our regression analysis may be slightly steeper. However, the accuracy of the $[\text{Cr}/\text{Zn}]$ and $[\text{Fe}/\text{Zn}]$ measurements is not sufficiently high to provide an unambiguous renormalization of one element to the other. Therefore $[\text{Fe}/\text{Zn}]$ and $[\text{Cr}/\text{Zn}]$ are used interchangeably in the present calculations.

i.e. their fractional ionization ratios remain constant along the sightline. In this case complex profiles can be modeled using the sum of the same number of components with identical centers and equal relative intensities for any pair of lines (Levshakov et al. 1999b).

The line profiles are described by the sum of m Voigt functions :

$$\tau_\lambda = \sum_{i=1}^m N_i \mathcal{V}[(\lambda - \lambda_0 - \lambda_0 \frac{v_i}{c})/\Delta\lambda_i], \quad (10)$$

where τ_λ is the optical depth at wavelength λ within the line profile, N_i is the column density in the i th component, v_i is its Doppler shift, and $\Delta\lambda_i = \lambda_0 b_i/c$ is its Doppler width with c being the speed of light and λ_0 the line center.

Equation (10) requires additional suggestion about the broadening mechanism. We assume that the main broadening is caused by bulk motion. For the component seen in the H₂ lines this suggestion is supported by the measured equivalence of b_{H_2} and b_{Me} , whereas for other components it is a model assumption which has to be checked during the optimization procedure.

Now we can describe our model in detail. It is fully defined by specifying $\{N_i\}_{i=1}^\kappa$ – the column density of the 1st components for each ion, with κ being the total number of ions ; $\{\mathcal{R}_{1i}\}_{i=2}^m$ – the relative intensities of the subcomponents, where for a given ion $\mathcal{R}_{1i} = N_i/N_1$; $\{v_i\}_{i=1}^m$ – the Doppler shifts ; and $\{b_i\}_{i=1}^m$ – the Doppler widths. All these parameters are components of the parameter vector $\theta = \{\theta_1, \theta_2, \dots, \theta_q\}$. In addition to θ , the D/H ratio is to be set. To estimate θ from the absorption line profiles, we minimize the objective function

$$\chi^2(\text{D/H}) = \frac{1}{\nu} \sum_{\ell=1}^L \sum_{i=1}^{M_\ell} [\mathcal{F}_{\ell, \lambda_i}^{\text{obs}} - \mathcal{F}_{\ell, \lambda_i}^{\text{cal}}(\theta)]^2 / \sigma_{\ell, i}^2, \quad (11)$$

where D/H is the total hydrogen isotopic ratio for the whole system. In (11), $\mathcal{F}_{\ell, \lambda_i}^{\text{obs}}$ is the observed normalized intensity of the spectral line ℓ , and $\sigma_{\ell, i}$ is the experimental error within the i th pixel of the line profile. $\mathcal{F}_{\ell, \lambda_i}^{\text{cal}}(\theta)$ is the calculated intensity of line ℓ at the same i th pixel having wavelength λ_i

$$\mathcal{F}_{\ell, \lambda_i}^{\text{cal}}(\theta) = \int e^{-\tau_{\ell, \lambda_i}(\theta)} \phi_{\text{PSF}}(\lambda_i - \lambda) d\lambda, \quad (12)$$

where $\tau_{\ell, \lambda_i}(\theta)$ is defined through Eq.(10). The instrumental point-spread function $\phi_{\text{PSF}}(\lambda)$ is approximated by a Gaussian with FWHM = 7.0 km s⁻¹ (see § 3.2).

The total number of spectral lines involved in the optimization procedure is labeled by L , and the total number of data points $\mathcal{M} = \sum_{\ell}^L M_\ell$, where M_ℓ is the number of data points for the ℓ th line. The number of degrees of freedom is labeled by ν .

After preliminary trial computations we were able to separate all available lines into two groups consisting of similar profiles (the fitting of each group of lines yielded acceptable χ^2 values). Similarity in this context means that the density weighted radial velocity distribution functions for elements combined in a group are equal [see eq.(15) and explanations below]. First group includes $\kappa = 9$ different ions (H I, C II, C II*, N I, O I, Si II, P II, Ar I, and Zn II) with the total number of data points $\mathcal{M} = 566$ and $\nu = 544$ (we consider C II* as a separate element since it has a column density different from C II). The second one consists of $\kappa = 2$ ions (Fe II and Cr II) with $\mathcal{M} = 110$, $\nu = 99$. These two groups are essentially the refractory and non- (or little) refractory elements.

We do not consider the absorption features seen at $\Delta v \simeq 40$ and 60 km s⁻¹ in the C II $\lambda 1036.3 \text{ \AA}$, N I $\lambda 1134.2 \text{ \AA}$, O I $\lambda 1039.2 \text{ \AA}$, and Si II $\lambda 1193.3 \text{ \AA}$ profiles (Figure 10) since we are mostly interested in the main H₂-bearing component ($\Delta v = 0$ km s⁻¹) and in the blue side parts of the profiles which restrict the configuration of the velocity field important for the analysis of the observed D I lines. For this reason only blue parts of the hydrogen H I Ly α , Ly-5, Ly-8, Ly-10, and Ly-12 lines were included in the analysis (see Figures 11 and 12). The components at $\Delta v \simeq 40$ and 60 km s⁻¹ increase the total column densities measured in the range $-50 \text{ km s}^{-1} \leq v \leq 80 \text{ km s}^{-1}$ at about 8% only.

The estimation of the parameter vector θ by means of the χ^2 -minimization is a typical *ill-posed* problem (Tikhonov & Arsenin 1977) because of the presence of two smoothing operators in (10) and (12) which prevent from deducing a unique value of θ . To stabilize the solution, we augment χ^2 by a regularization term in a way similar to that discussed in Levshakov et al. (1999b) – instead of minimizing χ^2 , defined in (11), we now seek the

minimum of another objective function,

$$\mathcal{L}_\alpha(\theta) = \chi^2(\theta) + \alpha \psi(\theta), \quad (13)$$

where ψ is a penalty function and α the regularization parameter.

The choice of ψ for nonlinear problems occurs rather heuristically. For our particular DLA we used additional information obtained from the analysis of H_2 . Namely, we searched for the minimum of $\mathcal{L}_\alpha(\theta)$ in the vicinity of the main component (i.e. $\Delta v_{\text{H}_2} \simeq 0 \text{ km s}^{-1}$) which is supposed to have $b \simeq b_{\text{H}_2}$. Then the easiest choice for ψ will be

$$\psi = \left(\frac{b - b_{\text{H}_2}}{\sigma_{b_{\text{H}_2}}} \right)^2 + (\Delta v - \Delta v_{\text{H}_2})^2, \quad (14)$$

and we set the regularization parameter $\alpha = 1$.

The importance of the regularization is illustrated in Figure 13, where different velocity distribution functions $p(v)$ are shown. The differences in shapes of $p(v)$ may cause different D/H values. For instance, being analyzed separately, the H+D profiles yield a shallow and smoother $p(v)$ (the dashed curve in Figure 13), whereas a simultaneous fitting with metals reveal a sharp spike at $\Delta v \simeq 0 \text{ km s}^{-1}$ (the solid curve) and a slightly different structure of the blue wing of $p(v)$ at $\Delta v < -5 \text{ km s}^{-1}$. The difference in D/H is, indeed, essential: D/H = $(2.24 \pm 0.67) \times 10^{-5}$ in the former case (see DDM), and D/H = $(3.75 \pm 0.25) \times 10^{-5}$ in the latter one (see Figure 14).

The estimated column densities together with their errors and relative abundances in the H_2 -bearing cloud are listed in Table 3. The errors were calculated by using the $\Delta\chi^2$ method. They reflect internal uncertainties of the physical parameters within the adopted model. Total column densities (calculated in the range $-50 \text{ km s}^{-1} \leq v \leq 20 \text{ km s}^{-1}$) for all elements, their relative abundances and corresponding errors are listed in Table 4. Besides, we also estimated in the main component 1σ upper limits to $N(\text{C I}) < 4.2 \times 10^{11} \text{ cm}^{-2}$ from the C I $\lambda 1277.2 \text{ \AA}$ line, to $N(\text{O I}^*) < 8.2 \times 10^{11} \text{ cm}^{-2}$ from the O I* $\lambda 1304.8 \text{ \AA}$ line, and to $N(\text{Si II}^*) < 2.6 \times 10^{12} \text{ cm}^{-2}$ from the Si II* $\lambda 1533.4 \text{ \AA}$ line using the Keck telescope spectrum of Q0347-3819 obtained by Prochaska & Wolfe (1999). These data are included in Table 3. The most probable b parameters, corresponding to the column densities from Table 3,

are as follows: $b_{\text{H I+Me}} = 2.71 \pm 0.05 \text{ km s}^{-1}$, and $b_{\text{Cr II+Fe II}} = 2.80 \pm 0.26 \text{ km s}^{-1}$. It shows that in spite of the difference in shapes of $p(v)$ for two groups of ions, the broadening parameter in the central H_2 -bearing component is the same.

The measured value of $\log N(\text{H I}) = 20.626 \pm 0.005 \text{ cm}^{-2}$ is in good agreement with the DDM measurement of $\log N(\text{H I}) = 20.63 \pm 0.09 \text{ cm}^{-2}$. The re-calculated value of D/H = $(3.75 \pm 0.25) \times 10^{-5}$ is consistent with standard big bang nucleosynthesis predictions (e.g. Burles et al. 1999) if the baryon-to-photon ratio, η , is in the range $4.37 \times 10^{-10} \lesssim \eta \lesssim 5.32 \times 10^{-10}$. With the present-day photon density determined from the CMBR (Mather et al. 1999), we can estimate the present-day baryon density $\Omega_b h_{100}^2 \equiv 3.73 \times 10^7 (T_{\text{CMBR}}/2.75)^3 \eta \simeq 0.016 \div 0.020$.

Our new D/H ratio is shifted toward the higher hydrogen isotopic ratio found in the Lyman Limit Systems (LLS) by Tytler et al. (2000), D/H = $(3.5 \pm 0.5) \times 10^{-5}$. We recall that the ratio of D/H $\simeq 4 \times 10^{-5}$ was found from the Tytler et al. LLSs using a different mesoturbulent method by Levshakov, Kegel, & Takahara (1998) and by Levshakov, Tytler, & Burles (2000). We thus summarize that when all most accurate measurements of D/H in high redshift QSO absorbers are considered, one finds the same D/H value which is about 2.5 times the mean ISM value of D/H = $(1.50 \pm 0.10) \times 10^{-5}$ (e.g. Linsky 1998).

To conclude this section, we comment on the fitting of the C II $\lambda 1036 \text{ \AA}$ line: the exact measurement of the column density for this ion is very important since the calculation of the volumetric gas density n_{H} in the $z_{\text{abs}} = 3.025$ molecular cloud is based on the ratio of $N(\text{C II}^*)/N(\text{C II})$. The C II $\lambda 1036 \text{ \AA}$ line is saturated and having this line alone we would be able to estimate only a lower boundary for $N(\text{C II})$. But the system under study exhibits a plenty of other metal profiles which are unsaturated. Being fitted together with C II, these profiles allow us to restrict the shape of the radial velocity distribution $p(v)$ and then to determine the real column density of C II. As already stated above, the measurement of $N(\text{C II})$ from the saturated $\lambda 1036 \text{ \AA}$ line is possible if the density weighted velocity distribution functions of C II and a match ion (which shows unsaturated absorption profiles) are equal.

Indeed, for a fixed value of λ (or v in the veloc-

ity space) within the line profile, the optical depth $\tau_{a,i}(\lambda)$ of element ‘a’ in the i th ionization stage is given by [cf. eqs. (24)-(26) in Levshakov, Agafonova, & Kegel 2000] :

$$\tau_{a,i}(\lambda) = k_0 N_{a,i} \int_0^1 n_{\text{H}}(x) \frac{\Upsilon_{a,i}[U(x)]}{\tilde{\Upsilon}_{a,i}} \times \Phi_{\lambda}[\Delta\lambda_{\text{D}}(x), v(x)] dx, \quad (15)$$

where k_0 is a constant for a particular line, $N_{a,i}$ the column density, $n_{\text{H}}(x)$ the volumetric gas density at point x , $\Upsilon_{a,i} = n_{a,i}/n_{\text{a}}$ the fractional ionization, $U = n_{\text{ph}}/n_{\text{H}}$ the ionization parameter with n_{ph} being the number of photons with energies above one Rydberg, Φ_{λ} the profile function at the local velocity $v(x)$, and $\tilde{\Upsilon}_{a,i}$ the mean density-weighted fractional ionization.

If the line broadening is caused by bulk motions and the ratio of the fractional ionizations for a pair of ions ‘a, i ’, ‘b, j ’ remains the same for all $U(x)$ along the sightline, then

$$\frac{\tau_{a,i}(\lambda)}{\tau_{b,j}(\lambda)} \propto \frac{N_{a,i}}{N_{b,j}} = \text{constant}. \quad (16)$$

Given the integral part of (15), which can be estimated from the unsaturated lines, we can easily calculate the column density for even saturated lines.

To test how accurately C II traces the distributions of other elements, we have studied the ionization properties of the warm H I gas assuming that it is embedded in an ionizing radiation field of given spectrum and intensity.

The CLOUDY code (Ferland 1996) was used to compute the fractional ionization of ions $\Upsilon_{a,i}$ as a function of the ionization parameter U . For a given value of n_{ph} , the fluctuation of U along the line of sight represents the reciprocal hydrogen density. We consider two limiting types of radiation fields: a hard, QSO-dominated spectrum representative of the radiation field external to the H₂-bearing cloud at $z = 3$ (Haardt & Madau 1996), and a soft, starlight background given by Mathis, Mezger, & Panagia (1983). For the chosen ionizing spectra, $n_{\text{ph}} = 2.2 \times 10^{-5} \text{ cm}^{-3}$ and $2.0 \times 10^{-6} \text{ cm}^{-3}$, respectively. Calculations were performed for metallicity $Z = 0.1Z_{\odot}$.

We found that most concordant with C II is the ion Si II which traces C II over a rather wide range of U . This is illustrated in Figure 15

where the ratios $\Upsilon_{\text{SiII}}/\Upsilon_{\text{CII}}$ and $\Upsilon_{\text{FeII}}/\Upsilon_{\text{CII}}$ (to stress the difference) are shown as functions of U . The displayed boundaries of U correspond to $n_{\text{H}} = 0.22 \div 2.2 \text{ cm}^{-3}$ (hard ionizing spectrum) and to $n_{\text{H}} = 0.02 \div 0.2 \text{ cm}^{-3}$ (soft ionizing spectrum). Figure 15 shows that $\Upsilon_{\text{SiII}}/\Upsilon_{\text{CII}}$ is practically constant for both ionizing fields. The behavior of $\Upsilon_{\text{FeII}}/\Upsilon_{\text{CII}}$ is, however, different: in both cases we may expect to observe non-similar profiles of the C II and Fe II lines.

Thus we can conclude from these calculation that independently on the background ionizing field the distribution of C II does trace the distribution of Si II in diffuse clouds ($0.1 \text{ cm}^{-3} \lesssim n_{\text{H}} \lesssim 10 \text{ cm}^{-3}$) and therefore we can use the unsaturated Si II profiles to measure $N(\text{C II})$ with a sufficiently high accuracy. In the present case we were able to describe with the same velocity distribution not only the C II and Si II lines, but profiles of the other elements. This fact seems to justify the suggestion that the density fluctuations in the H₂ cloud are rather small and thus the derived $N(\text{C II})$ value can be considered as reliable.

4. Discussion

We turn now to the question of the physical conditions in the $z_{\text{abs}} = 3.025$ DLA. The measured column densities of metals and H₂ can be used to estimate the volumetric gas density and the intensity of the UV radiation field. We begin with the metal absorptions. Then we consider if the observed H₂ distribution over the excited rotational states can be described with metals in a self-consistent way. After that we compare the revealed [α -element/iron-peak] ratio and abundances with those known from different DLAs.

4.1. Metal absorption from the ground and excited states

The absorption lines from the fine-structure levels of atoms and ions provide comprehensive information about the physical properties in the DLAs (e.g., Bahcall & Wolf 1968; Silva & Viegas 2001).

In equilibrium, the population ratio of the upper level n_2 to the lower level n_1 , in ions with a doublet fine structure in the ground state, is given

by

$$\frac{n_2}{n_1} \simeq \frac{Q_{1,2} + w_{1,2}}{A_{2,1}}, \quad (17)$$

where $w_{1,2}$ and $Q_{1,2}$ are the photon absorption and the collisional excitation rates, respectively, and $A_{2,1}$ is the radiative transition probability.

In the present analysis, we are interested mainly in the physical conditions in the gas where both the H₂ and the metal absorptions have been detected. We assume that this absorbing region is homogeneous and therefore the number density ratios are equal to the corresponding ratios of column densities, $n_2/n_1 = N_2/N_1$. We neglect fluorescence since this indirect excitation process has usually lower rates as compared to the direct collisional excitations and/or the IR radiative absorption rates. The radiative decay and the de-excitation rates are also ignored since in our case they have low efficiency.

In the main component of the $z_{\text{abs}} = 3.025$ system the following quantities were estimated from the data listed in Table 3: $N(\text{H I}) = (2.521 \pm 0.035) \times 10^{20} \text{ cm}^{-2}$, $N(\text{C II}) = (5.05 \pm 0.28) \times 10^{15} \text{ cm}^{-2}$, $\text{C II}^*/\text{C II} = (4.5 \pm 0.3) \times 10^{-3}$, $\text{C I}/\text{C II} < 8 \times 10^{-5}$, $\text{O I}^*/\text{O I} < 3 \times 10^{-5}$, and $\text{Si II}^*/\text{Si II} < 2 \times 10^{-3}$.

The ground state of the C⁺ ion consists of two levels $2s^2 2p^2 \text{P}_{1/2,3/2}^0$ with the energy difference of $\Delta E = 91.32 \text{ K}$ and the spontaneous decay rate of $A_{2,1} = 2.291 \times 10^{-6} \text{ s}^{-1}$. The excited $J = 3/2$ level may be populated by collisions with electrons, e⁻, hydrogen atoms, H⁰, protons, H⁺, and molecules, H₂. Among them the highest rate is found for collisions with electrons: $Q_{1,2}^{e^-} \simeq 2 \times 10^{-7} n_e \text{ s}^{-1}$ in the range $10^2 \text{ K} < T_{\text{kin}} < 10^3 \text{ K}$ (see, e.g., Figure 3 in Silva & Viegas 2001). But the electron density in H I regions comes mainly from the photoionization of carbon, $n_e \simeq (\text{C}/\text{H}) n_{\text{H}}$, which is approximately equal to $3 \times 10^{-5} n_{\text{H}}$ for the $z_{\text{abs}} = 3.025$ DLA. Then $Q_{1,2}^{e^-} \simeq 6 \times 10^{-12} n_{\text{H}} \text{ s}^{-1}$ becomes lower than the H⁰-C⁺ collisional rate for the same temperature interval where $Q_{1,2}^{\text{H}^0}$ is almost constant and equals $Q_{1,2}^{\text{H}^0} \simeq 1.45 \times 10^{-9} n_{\text{H}} \text{ s}^{-1}$ (Launay & Roueff 1977a). The rate of the photon absorption in the $z_{\text{abs}} = 3.025$ DLA is mainly induced by the cosmic microwave background radiation (Molaro et al. 2001b) and equals to $w_{1,2} \simeq 1.1 \times 10^{-9} \text{ s}^{-1}$.

From (17) and taking the limiting values of the measured C II*/C II ratio, one obtains $n_{\text{H}} \simeq 6 \div 7$

cm^{-3} . The low limit of $n_{\text{H}} \gtrsim 4 \text{ cm}^{-3}$ stems from the analysis of the H₂ lines (see § 4.2).

To check the consistency of the estimated n_{H} with other metal absorption lines, we can use the upper limits to the column densities of O I* and Si II*. The equilibrium equation for the three-level system (³P₂, ³P₁, ³P₀ states of O⁰) can be written as (cf. Molaro et al. 2001a)

$$\frac{n_1}{n_0} \simeq \frac{(Q_{0,1}^{\text{H}^0} + Q_{0,2}^{\text{H}^0})}{A_{1,0}}, \quad (18)$$

where the subscripts 0, 1, and 2 denote the ground (0) and excited (1,2) levels, respectively. The spontaneous decay rate $A_{1,0} = 8.95 \times 10^{-5} \text{ s}^{-1}$, and the energy differences between the ground state and the corresponding fine-structure levels are $\Delta E_{0,1} = 228 \text{ K}$ and $\Delta E_{0,2} = 326 \text{ K}$.

If n_e is small, the rate coefficient for collisions with hydrogen atoms is dominating. At the kinetic temperature $T_{\text{kin}} = 400 \text{ K}$, we find from Launay & Roueff (1977b) $Q_{0,1}^{\text{H}^0} = 1.65 \times 10^{-11} n_{\text{H}} \text{ s}^{-1}$ and $Q_{0,2}^{\text{H}^0} = 0.10 \times 10^{-11} n_{\text{H}} \text{ s}^{-1}$. Then (18) yields $n_{\text{H}} < 150 \text{ cm}^{-3}$, which is consistent with the foregoing value.

The fine-structure level of the Si⁺ ion (³P_{3/2}⁰) has an effective excitation temperature $\simeq 414 \text{ K}$ which means that the estimated upper limit to $N(\text{Si II}^*)$ is less sensitive to low gas densities in this last case. Besides, absorption features produced by Si II* must come only from H II regions as argued by Spitzer & Jenkins (1975). The absence of the Si II* absorption might indicate that there is no dense H II gas region on the line of sight. This suggestion is also supported by the absence of the N II* $\lambda 1084.562 \text{ \AA}$ and $\lambda 1084.580 \text{ \AA}$ lines in the $z_{\text{abs}} = 3.025$ system. Both facts show that the C II* and C II absorptions arise predominantly in a warm H I gas in agreement with our model described in § 3.6.

4.2. H₂ distribution over the rotational states

We find no pronounced differences between the H₂ abundances in the $z_{\text{abs}} = 3.025$ DLA system and in the Galactic diffuse clouds which have comparable H I column densities. The high excitation temperature in our system, $T_{\text{ex}} = 825 \pm 110 \text{ K}$, is also consistent with previous observations in the Galaxy. For instance, in a pioneer work by

Spitzer & Cochran (1973) it has been shown that $T_{\text{ex}} > 300$ K within diffuse interstellar clouds where the H_2 column density in the $J = 0$ rotational level $N(0) < 10^{15} \text{ cm}^{-2}$, and the temperature as high as 1100 K has been detected by Morton & Dinerstein (1976) toward ζ Pup.

It has been discussed in §3.4 that the populations in the excited rotational states of H_2 cannot be supported only by collisions in a gas whose kinetic temperature is as high as 800 K. We calculated the H_2 collisional excitation rates by using the analytical approximations given in Shull & Beckwith (1982). The deduced rates are listed in Table 5, columns 3 and 4 for $T_{\text{kin}} = 400$ K and 1000 K, respectively. In columns 5 and 6 we show, for comparison, the rates obtained in different models by Nishimura (1968) and Elitzur & Watson (1978). As noted by Shull & Beckwith, the accuracy of the collisional excitation rates are not sufficiently high and different models may produce deviations of about 50%. The employed analytical fit to the H^0 - H_2 excitation rates agrees with the Elitzur & Watson calculations to better than 25 %, but gives much lower values than the Nishimura rates. The radiative rates listed in column 2 were taken from Turner, Kirby-Docken, & Dalgarno (1977).

The collisional excitation of the $J = 3$ level is not expected to be effective in our case. Indeed, the $J = 2$ level has longer radiative lifetime when compared with the $J = 3$ level ($t_{J=2} = 3.4 \times 10^{10}$ s and $t_{J=3} = 2.1 \times 10^9$ s, respectively), and therefore the $J = 2$ level is more sensitive to the collisional de-excitation. The critical density, $n_{\text{H}}^{\text{cr}} = A_{2 \rightarrow 0}/q_{2 \rightarrow 0}$, above which collisional de-excitation becomes important is $n_{\text{H}}^{\text{cr}} = 3.6 \text{ cm}^{-3}$. Thus, $n_{\text{H}} \gtrsim 4 \text{ cm}^{-3}$ is required to maintain the observed $N(2)/N(0)$ ratio at $T_{\text{kin}} = 400$ K. The absence of a fracture at lower J in the graph $\log[N(J)/g(J)]$ versus $E(J)$, shown in Figure 8, can be used to infer an upper limit for the gas density, $n_{\text{H}} \lesssim 74 \text{ cm}^{-3}$. Both limits are consistent with n_{H} estimated from the measured $N(\text{C II}^*)/N(\text{C II})$ ratio.

Now we can set restrictions on the rate of photo-dissociation, I , in the $z_{\text{abs}} = 3.025$ molecular cloud assuming that the H_2 molecules are formed on grains with rate R and partly destroyed through the fluorescence process. In equilibrium, the fractional molecular abundance is given by

$$(Jura 1974) \quad f_{\text{H}_2} \simeq 2Rn_{\text{H}}/I. \quad (19)$$

To estimate the rate of formation of H_2 , we use the approximation from Black & Dalgarno (1977)

$$R \simeq 10^{-6} T_{\text{kin}}^{0.5} n_{\text{H}} n_{\text{d}} \text{ cm}^3 \text{ s}^{-1}. \quad (20)$$

Here the number density of dust grains, n_{d} , is related to the total hydrogen density, n , through

$$n_{\text{d}} = 10^{-12} n = 10^{-12} (n_{\text{H}} + 2n_{\text{H}_2}), \quad (21)$$

which is the usual relation for the interstellar diffuse clouds.

Then, accounting for the dust-to-gas ratio $\tilde{k} \simeq 0.05$ (see § 3.5) and the fact that $n_{\text{H}_2} \ll n_{\text{H}}$ in the $z_{\text{abs}} = 3.025$ cloud, we find

$$R \simeq 10^{-18} T_{\text{kin}}^{0.5} \tilde{k} n_{\text{H}}^2 \simeq 5 \times 10^{-20} T_{\text{kin}}^{0.5} n_{\text{H}}^2 \text{ cm}^3 \text{ s}^{-1}. \quad (22)$$

Then for $T_{\text{kin}} = 400$ K, H_2 forms at a rate $R \simeq 1.0 \times 10^{-18} n_{\text{H}}^2 \text{ cm}^3 \text{ s}^{-1}$.

This value of R will be consistent with the upper limit found by Jura (1974) in the Galactic ISM, $R_{\text{G}} \lesssim 2 \times 10^{-16} \text{ cm}^3 \text{ s}^{-1}$, if $n_{\text{H}} \lesssim 14 \text{ cm}^{-3}$ at $z_{\text{abs}} = 3.025$. By this we confine n_{H} in the interval $4 \text{ cm}^{-3} \lesssim n_{\text{H}} \lesssim 14 \text{ cm}^{-3}$ which provides a self-consistency between the observed $N(2)/N(0)$ ratio and the maximum formation rate of H_2 under the condition that the physical properties of the dust grains in the Milky Way and at $z_{\text{abs}} = 3.025$ are similar.

Since the molecular hydrogen fractional abundance in the main component of the $z_{\text{abs}} = 3.025$ absorber is $f_{\text{H}_2} = (3.3 \pm 0.2) \times 10^{-6}$, cloud parameters $n_{\text{H}} \simeq 6 \text{ cm}^{-3}$ and $T_{\text{kin}} = 400$ K will yield $I \simeq 2 \times 10^{-10} \text{ s}^{-1}$ which agrees well with the values measured in the interstellar clouds containing optically thin H_2 : $0.5 \times 10^{-10} \text{ s}^{-1} \leq I_{\text{G}} \leq 16.0 \times 10^{-10} \text{ s}^{-1}$ (Jura 1975a). Thus, the radiation field in the $z_{\text{abs}} = 3.025$ cloud is quite comparable with those measured in transparent interstellar clouds in the MW.

We now evaluate the total hydrogen density, n_{H} , the photo-absorption rate, β_0 , and the steady state production rate of molecular hydrogen, R , from the relative population of the different rotational levels of H_2 . Our analysis is, in general, the same as described by Spitzer & Zweibel (1974) and by Jura (1974, 1975a,b). However,

we re-calculated the formation efficiency coefficients ε_4 and ε_5 for the $J = 4$ and 5 levels including upper rotational levels with a cutoff above $J_{\max} = 15$. These coefficients were calculated from the Boltzmann distribution of molecules formed upon grain surfaces with an effective temperature, T_f (for details, see Black & Dalgarno 1976). Since a newly formed molecule quickly cascades to the ground vibrational level, we assume that the newly formed molecules populate the ($v=0$, $J=4$) and ($v=0$, $J=5$) levels. It is usually assumed that molecules are formed at $T_f \simeq 17400$ K, which is the temperature equivalent of the binding energy of H_2 distributed statistically among the rotation-vibration levels upon formation (e.g. Spitzer & Zweibel 1974). Then we find $\varepsilon_4 = 0.21$ and $\varepsilon_5 = 0.65$ (cf. $\varepsilon_4 = 0.19$ and $\varepsilon_5 = 0.44$ from Jura 1975b).

The concentrations of H_2 in the $J = 4$ and 5 levels may be approximately estimated from the statistical equilibrium equations

$$A_{4+K,2+K} n_{4+K} = \varepsilon_{4+K} R n_H^2 + \beta_0 \sum_{J'} p_{4+K,J'} n_{J'} , \quad (23)$$

where $J' = K, K+2, K+4$, and $K = 0$ or 1 for $J = 4$ or 5 , respectively.

In these equations, the pumping efficiency coefficients $p_{i,j}$ are taken from Jura (1975a). The quantity $p_{i,j}$ shows the probability (averaged over the different Lyman and Werner bands) that photo-absorption from the j th rotational level will lead to the population of the i th rotational level in the ground $v = 0$ vibrational state.

From (23) we can calculate $R n_H$ using the measured $N(4)/N(H)$ and $N(5)/N(H)$ ratios. It gives $R n_H \simeq 3 \times 10^{-16} \text{ s}^{-1}$. If we take $R \simeq 5 \times 10^{-17} \text{ cm}^3 \text{ s}^{-1}$ from Spitzer & Cochran (1973), then $n_H \simeq 6 \text{ cm}^{-3}$. Now the H_2 destruction rate can be estimated from (19) which gives again $I \simeq 2 \times 10^{-10} \text{ s}^{-1}$ as in the foregoing estimations. If $I \simeq 0.11\beta_0$ (Jura 1974), then the rate of photo-absorption is $\beta_0 \simeq 2 \times 10^{-9} \text{ s}^{-1}$. On the other hand, the average β_0 for the intergalactic UV background at $z \simeq 3$ is about $2 \times 10^{-12} \text{ s}^{-1}$ (Srianand & Petitjean 1998), while the MW interstellar radiation field value ranges between $5 \times 10^{-10} \text{ s}^{-1} \leq \beta_0 \leq 16 \times 10^{-9} \text{ s}^{-1}$ (Jura 1975a). Thus, our measurements show a close similarity with the average characteristics of the UV field found in the

MW.

For the neutral hydrogen column density $N(H\text{ I}) \simeq 2.5 \times 10^{20} \text{ cm}^{-2}$ and $n_H \simeq 6 \text{ cm}^{-3}$, the linear size of the H_2 -bearing cloud along the line of sight is equal to $D \simeq 14 \text{ pc}$ which yields a mass of $M \simeq 0.5 D^3 n_H m_H \simeq 200 M_\odot$, assuming spherical geometry.

4.3. [α -element/iron-peak] ratios

The elemental column densities obtained following the procedure described in sections 3.5 and 3.6 together with the relative abundances are summarized in Table 4.

Among the elements belonging to the iron-peak group, Zn is a good indicator of the absolute metal abundance in the system, since Zn is known to be essentially undepleted in the ISM (Pettini et al. 1999). Measurements of Zn in high redshift systems have been proven to be very challenging since the Zn II resonance lines fall at wavelengths $> 8000 \text{ \AA}$ where spectrograph and CCD efficiency decrease while sky emissivity increases. The Zn measurement presented here and that in the DLA at $z_{\text{abs}} = 3.39$ toward Q0000–2621 are the only ones obtained for systems with $z \geq 3$. The derived $[Zn/H] = -1.50 \pm 0.05$ is in line with the bulk of $[Zn/H]$ measurements found in the redshift interval $2 < z < 2.5$ although higher by 0.6 dex than that of the DLA at $z_{\text{abs}} = 3.39$ toward Q0000–2621 confirming the presence of significant spread in absolute abundance in DLA with comparable redshifts. The straight mean of the Zn measurements in the redshift interval from $2 \leq z \leq 3$ is $[Zn/H] \approx -1.2$, and does not differ from the column density weighted mean for the same redshift interval (Vladilo et al. 2000). This new measurement therefore supports the general metallicity behavior, characterized by the intrinsic spread for a given redshift and by a mild trend of increasing abundance with the decreasing redshift if not a lack of evolution when the hydrogen column density weighted mean is considered.

As described in previous § 3.6, our model keeps the constant ratio between the matching components. With this condition imposed, we cannot account for different chemical abundances or the presence of different dust pattern depletion among the components of the system. It may be possible that a contribution from warmer gas or different

dust depletion is responsible for the observed difference in profile shapes of Fe II and other ions.

Only recently it became possible to measure oxygen with an acceptable accuracy using the fainter O I lines falling in the Ly α forest instead of the always strongly saturated O I λ 1302 Å transition (Lopez et al. 1999; Molaro et al. 2000; Dessauges-Zavadsky et al. 2001). In the present paper, the O abundance is derived from the set of eleven OI lines used either for direct fitting or just for the consistency test.

The [O/Zn] is the most informative ratio to trace back the kind of chemical evolution of the absorber. Both elements show little affinity with dust grains and are good representatives of α -chain and iron-peak elements, respectively. If the system is in the early stages of chemical evolution, the relative abundances should reflect the yields of Type II SNe characterized by the enhancement of α -elements. In fact, it was rather surprising to find little evidence for this enhancement when elements such as S and Si, once corrected by dust, were used in combination with Zn (Centurión et al. 2000; Vladilo 1998) and the ratio [O/Zn] = 0.1 has been measured in the DLA toward Q0000–2621 (Molaro et al. 2001a).

The ratio [O/Zn] = 0.68 ± 0.08 , found here, represents the first clear cut evidence for a genuine enhancement of the α -elements comparable to that observed in the metal poor stellar population of the Milky Way (Israelian et al. 2001). The oxygen result is also supported by the other α -elements we have been able to measure, namely [Ar/Zn] = 0.34 ± 0.07 , [Si/Zn] = 0.56 ± 0.06 , and [S/Zn] = 0.41 ± 0.08 (if we take $\log N(\text{S II}) = 14.73 \pm 0.01 \text{ cm}^{-2}$ from Prochaska & Wolfe 1999). Argon abundance is slightly below the values obtained from the other α -elements, but this is not surprising since Ar is sensitive to photoionization effects and shows in the Galaxy even larger depletion factors (Sofia & Jenkins 1998).

All results available at present allow us to conclude that the DLAs probably comprise a mix of chemical abundance pattern with both low and *standard* α -element enhancement. It is not clear at the moment if this reflects the different enrichment histories or just the same type of galaxies caught at different stages of their chemical evolution. It is interesting to note that estimated in the H₂-bearing cloud the ratio (Ar/O) = -2.65

is comparable to that observed in the DLA toward Q0000–2621, (Ar/O) = -2.25 (Molaro et al. 2001a), in particular when allowing for a small degree of Ar photoionization. As argued by Henry & Worthey (1999) the similarity of these ratios in a variety of galactic systems from the MW to Blue Compact galaxies strengthens the case for the existence of a universal IFM.

It is commonly assumed that nitrogen is mostly produced by the intermediate massive stars (Henry, Edmunds, & Köppen 2000). In DLAs, N shows a scatter well in excess of observational uncertainties which has been interpreted as being due to the delayed release of N compared to O (Centurión et al. 1998). Our value in the ‘[O/H]–[N/O]’ plane has coordinates [O/H] = -0.82 and [N/O] = -0.84 and falls close to the line for a pure secondary origin for N (cf. Figure 8 in Centurión et al. 1998). If intermediate massive stars had not yet time to evolve and to contribute to the N enrichment then this sets an upper limit of approximately 10^8 yr to the evolutionary age of the $z_{\text{abs}} = 3.025$ system. The young age of the system under study is also consistent with the observed α -element enhancement.

Phosphorus has been measured in the DLA toward Q0000–2621 (Molaro et al. 2001a) and toward Q1759+7539 (Outram et al. 2000). P cannot be measured in halo stars and thus the damped Ly α systems provide a unique astrophysical site where this element can be measured in low metallicity environments. Our determination is based only on the P II λ 963.8 Å line and may be slightly overestimated due to H I contamination. We have here the mean value of [P/Si] ≈ -0.2 which suggests the presence of a moderately odd-Z/even-Z effect which is a common feature in all P measurements in DLAs so far.

5. Conclusions

The main results of this paper are as follows.

(1) In the high resolution UVES spectrum of the quasar 0347–3819 we have identified over 80 absorption features with the Lyman and Werner lines arising from the J = 0 to 5 rotational levels of the ground electronic-vibrational state of H₂. These lines belong to the $z_{\text{abs}} = 3.025$ damped Ly α system.

(2) The application of the standard Voigt fit-

ting analysis to the main subcomponent at $z_{\text{H}_2} = 3.024855 \pm 0.000005$ gives the total H_2 column density of $N(\text{H}_2) = (4.10 \pm 0.21) \times 10^{14} \text{ cm}^{-2}$ and the Doppler width $b_{\text{H}_2} = 2.80 \pm 0.45 \text{ km s}^{-1}$. The kinetic gas temperature is less than 430 K.

(3) The fractional abundance of H_2 in the main component is equal to $f_{\text{H}_2} = (3.3 \pm 0.2) \times 10^{-6}$, while being compared to the total H I column density it yields $f_{\text{H}_2} = (1.94 \pm 0.10) \times 10^{-6}$. These values are similar to those observed in the ISM diffuse clouds with low color excesses, $E(B - V) < 0.1$. Using the total hydrogen column density in the main component $N(\text{H I}) \simeq 2.5 \times 10^{20} \text{ cm}^{-2}$ and the approximate relationship $N(\text{H}) \simeq 7.5 \times 10^{21} E(B - V) \text{ cm}^{-2} \text{ mag}^{-1}$, which assumes that the gas and dust grains are uniformly mixed (Spitzer & Jenkins 1975), we obtain $E(B - V) \simeq 0.03 \text{ mag}$ in the H_2 -bearing cloud. For the second strong component with $N(\text{H I}) \simeq 1.5 \times 10^{20} \text{ cm}^{-2}$ at $\Delta v \simeq -17 \text{ km s}^{-1}$ we set a very low limit to $f_{\text{H}_2} < 3.3 \times 10^{-9}$ (3σ). The $z_{\text{abs}} = 3.025$ system is not a homogeneous cloud but rather a mixture of cold and warm gas.

(4) The total column densities in the ortho and para- H_2 states yield the ratio $N_{\text{ortho}}/N_{\text{para}} = 3.1 \pm 0.3$ which is close to 3:1 expected from the hot H_2 formation upon grain surfaces. Similar ratios of 2.4 ± 0.9 and 3.1 ± 0.8 are estimated at $z_{\text{abs}} = 2.33771$ and 2.8112 toward Q1232+0815 and Q0528-250 from the published data by Srikanand et al. (2001) and Srikanand & Petitjean (1998), respectively. These ratios are, however, higher than the ‘freeze-out’ ortho:para- $\text{H}_2 = 1:4$ predicted for the early universe at $z < 20$ (Flower et al. 2000). It appears that H_2 detected in these three DLAs has undergone a re-forming phase in the period between $z \simeq 20$ and $z \simeq 3$ ($\Delta t \simeq 2 \text{ Gyr}$).

(5) We found that the population of the low rotational levels can be represented by a single excitation temperature of $T_{\text{ex}} = 825 \pm 110 \text{ K}$. Such high T_{ex} agrees well with the results by Spitzer & Cochran (1973) who showed that $T_{\text{ex}} > 300 \text{ K}$ within diffuse clouds which have $N(\text{J} = 0) < 10^{15} \text{ cm}^{-2}$, as it is in our case.

(6) From the measured $[\text{Cr}/\text{H}]$ and $[\text{Zn}/\text{H}]$ ratios we calculated the gas-to-dust ratio $k = 0.032 \pm 0.005$ in the whole $z_{\text{abs}} = 3.025$ system (the ratio $[\text{Cr}/\text{Zn}]$ is usually used to indicate the presence of dust in DLAs). The derived H_2 fractional

abundance fits well in the linear relation between $\log f_{\text{H}_2}$ and $[\text{Cr}/\text{Zn}]$ supporting our previously obtained results for other DLA systems (Levshakov et al. 2000b).

(7) From the observed population ratios of H_2 in different rotational states and the C II*/C II ratio we inferred the hydrogen number density n_{H} in the H_2 -bearing cloud $n_{\text{H}} \simeq 6 \text{ cm}^{-3}$, and the cloud dimension along the line of sight $D \simeq 14 \text{ pc}$ which gives $M \simeq 200 M_{\odot}$.

(8) From the relative populations of H_2 in the J = 4 and 5 rotational levels we estimated the rate of photo-destruction $I \simeq 2 \times 10^{-10} \text{ s}^{-1}$. The photo-absorption rate, $\beta_0 \simeq I/0.11$, is thus equal to $\beta_0 \simeq 2 \times 10^{-9} \text{ s}^{-1}$. Taking into account that the MW interstellar radiation field value ranges in $5 \times 10^{-10} \text{ s}^{-1} \leq \beta_0 \leq 16 \times 10^{-9} \text{ s}^{-1}$ (Jura 1975a), we conclude that the UV radiation fields in the $z_{\text{abs}} = 3.025$ absorbing cloud and in the Galactic ISM are very much alike. We also found that the formation rate of H_2 upon grain surfaces, $R n_{\text{H}} \simeq 3 \times 10^{-16} \text{ s}^{-1}$, is similar to that found in the Galaxy by Jura.

(9) The metal abundances from the $z_{\text{abs}} = 3.025$ DLA reveal a pronounced [α -element/iron-peak] enhancement with $[\text{O}, \text{Si}/\text{Zn}] = 0.6 \pm 0.1$ at the 6σ confidence level, the first time that this abundance pattern is unambiguously identified in a DLA system. The same order of magnitude enrichment of α -chain elements has been observed in Galactic metal-poor stars. The measured $[\text{N}/\text{O}]$ ratio implies the chemical history age of this DLA of $\lesssim 10^8 \text{ yr}$.

(10) The analysis of the metal profiles combined with the H+D Lyman series lines yields a new estimation of the hydrogen isotopic ratio $\text{D}/\text{H} = (3.75 \pm 0.25) \times 10^{-5}$ in this DLA. It implies for the baryon-to-photon ratio, η , a value in the interval $4.37 \times 10^{-10} \lesssim \eta \lesssim 5.32 \times 10^{-10}$, and the present-day baryon density $\Omega_{\text{b}} h^2 \simeq 0.016 \div 0.020$, which is in good agreement with a new analysis of the BOOMERANG experiment yielding $\Omega_{\text{b}} h^2 = 0.021 \pm 0.003$ (Netterfield et al. 2001).

S.A.L. gratefully acknowledges the hospitality of the European Southern Observatory (Garching), Osservatorio Astronomico di Trieste, and the National Astronomical Observatory of Japan (Mitaka) where this work was performed. We also

thank A. Wolfe & J. X. Prochaska for making available the calibrated Keck/HIRES spectrum of Q0347–3819, and I. I. Agafonova for many valuable comments on data analysis. We are greatly indebted to our referee for noting a shortcoming in the pipeline software and for helpful comments. The work of S.A.L. is supported in part by the RFBR grant No. 00-02-16007.

A. Correlated measurements

In order to evaluate the uncertainties in the derived physical parameters, one must know the standard errors, σ_j , for all the data points. These errors, computed through the UVES data reduction pipeline (Ballester et al. 2000) are not, however, statistically independent. The pipeline data resampling to constant wavelength bins introduces a correlation between the data point values. Besides the resampling procedure can change statistical properties of the noise (e.g., the simplest linear interpolation scheme smooths the random noise since the uncertainty of the data point value half way between two measurements is less than that for the real detector amplitudes at the limiting points).

Data point correlation is clearly seen in Figure 7 where the sequences of points at the continuum level (e.g., panels L2-0R0 or L2-0P3) show that neighboring points differ from each other by less than σ_j (for the data shown in Figure 7, the correlation coefficient $r \simeq +0.77$). The correlation length, ξ , of about 1.5 bin can be deduced from the analysis of the autocorrelation function (ACF)¹¹ of the intensity fluctuations in the continuum windows free from absorption-line features. This ACF is shown by histogram in Figure 16a where an exponential correlation function $f(\Delta n) = \exp(-\Delta n/\xi)$ of the simplest data model, – the first order autoregression (the Markov process), – is overdrawn by the smooth curve (here Δn is the scale shift).

The correlated data make the standard $\Delta\chi^2$ calculation of parameter confidence intervals questionable. To investigate this point we performed the following Monte Carlo (MC) analysis in combination with the least-squares method.

It is well known that the least-squares method (LSM) is computationally equivalent to the χ^2 -minimization (e.g., Meyer 1975). It is also known that the LSM is an unbiased and minimum variance estimator (Gauss-Markov theorem) irrespective of the distribution of the measurements including correlated data as well (Aitken 1934). Therefore, in the MC analysis, we used the best fitting parameters (the parameter vector $\hat{\theta}$, see § 3.6) found by means of the standard χ^2 -minimization, and calculated uncertainties of the $\hat{\theta}$ -components in the vicinity of the global minimum of the objective function by using the MC procedure.

Our computational MC procedure consists of the following steps:

- (1) A simulation box in the parameter space is specified by fixing the parameter boundaries $\hat{\theta}_i(1 - \beta) < \theta_i < \hat{\theta}_i(1 + \beta)$; in our case $\beta = 0.3$.
- (2) Initial guess $\theta^{(0)}$ is chosen arbitrary within the simulation box.
- (3) A random realization of the ‘observational’ points is generated in the following way: the j th data point value is altered with a probability P by means of the relation

$$\mathcal{F}_j^{\text{rnd}} = \mathcal{F}_j^{\text{obs}} + \sigma_j g,$$

where g is a random normal variable with zero mean and unit dispersion, and $\mathcal{F}_j^{\text{obs}}$ is the normalized observational intensity¹² in the j th bin ($j = 1, 2, \dots, \mathcal{N}$; with \mathcal{N} being the total number of data points).

- (4) Objective function is minimized and all solutions with $\chi^2 < 1.10$ are collected.
- (5) The whole procedure is repeated many times to collect a representative sample (i.e. the number of measurements $\mathcal{K} > 30$). Then the sample mean and standard deviation are calculated.

To compare both $\Delta\chi^2$ and MC results we carried out the MC procedure for the b parameter and the H_2 abundances at different J levels. Nineteen H_2 lines (L3-0R0, L7-0R0, L1-0P1, L3-0P1, L14-0P1, W0-0R2, W0-0Q2, L3-0R2, L4-0R2, L5-0R2, L2-0R3, L2-0P3, L3-0P3, L4-0R3, L15-0R3, L5-0R4, L8-0P4, L7-0P5, L12-0R5; see Figs. 5 and 6) have been chosen and fitted simultaneously with the individual Gaussian profiles. The obtained estimations (for $\mathcal{N} = 177$ and $\mathcal{K} = 181$) summarized in Table 6 show that in this case $\Delta\chi^2$ yields

¹¹ The ACF is defined, e.g., in Bendat & Piersol (1971)

¹² This randomization decreases the correlation between consecutive bins, but increases the noise. For instance, if $P = 0.7$ the correlation length equals $\xi \simeq 1.0$ bin (see Figure 16b) but the noise level is about a factor of $\sqrt{2}$ higher.

practically the same mean values but systematically higher standard deviations. Since statistical properties of the noise are not exactly known we use in the present paper the most conservative $\Delta\chi^2$ estimations of the standard deviations and of the mean values.

B. Metal systems toward QSO 0347–3819

We have thoroughly investigated all possible coincidences of H₂, H I, D I, and metal absorption features from the $z_{\text{abs}} = 3.025$ damped Ly- α system with metal absorptions from other systems observed toward Q0347–3819. Positions of the found blends are indicated in Figures 5, 6, 10, and 11. The strongest systems detected in the spectral ranges $\lambda\lambda = 3680 - 4880 \text{ \AA}$, $4880 - 6730 \text{ \AA}$ (this portion of the spectrum obtained at the Keck telescope was kindly shared with us by Wolfe & Prochaska), $6730 - 8520 \text{ \AA}$, and $8685 - 10000 \text{ \AA}$ are listed below. Since almost all identified metal profiles exhibit complex structures, the quoted redshifts are the ones of the strongest components or the average redshifts in the cases when the components are not well separated. In cases where the hydrogen Ly- α line lies outside the observable spectral range, we consider a doublet of absorption lines caused by the same ion as an individual metal system if the lines show identical profile shapes. The identifications made in the $z_{\text{abs}} = 3.025$ DLA are not included in the list. Possible blends are shown in parenthesis.

$z_1 = 0.000019$	Ca II 3934,3969(+W1-0R2)
$z_2 = 1.4579$	Mg I 2852; Mg II 2796,2803; Al II 1670; Al III 1854; Si II 1526,1808; Fe II 1608,2260,2344,2374,2382,2586,2600
$z_3 = 1.5159$	C IV 1548,1550
$z_4 = 1.5263$	Mg II 2796,2803; Si II 1526(+Ly- γ z_{15}),1808; Fe II 2344,2382,2600
$z_5 = 1.6768$	C IV 1548,1550
$z_6 = 2.2140$	Ly- α ; C II 1334; C IV 1548,1550; O I 1302; Mg II 2796,2803; Al II 1670; Al III 1854; Si II 1190(+W3-0Q3),1193,1260; Si III 1206; Si IV 1393,1402; Fe II 1608,2344,2374,2382,2586,2600
$z_7 = 2.3932$	Ly- α (+Ly- β DLA); C IV 1548,1550
$z_8 = 2.4344$	Ly- α ; C IV 1548,1550
$z_9 = 2.5371$	Ly- α ; C II 1334; C IV 1548,1550; Al II 1670; Si II 1260; Si IV 1393
$z_{10} = 2.6504$	Ly- α ; C IV 1548,1550; Si III 1206; Si IV 1393,1402
$z_{11} = 2.6526$	Ly- α ; C IV 1548,1550; Si III 1206; Si IV 1393,1402
$z_{12} = 2.8102$	Ly- α ; C II 1334; Si II 1190,1193,1260(+Si II 1193 DLA); Si IV 1393,1402
$z_{13} = 2.8483$	Ly- α , Ly- β (+Ly- γ z_{19}); C III 977; C IV 1548,1550
$z_{14} = 2.8992$	Ly- α , Ly- β , Ly- γ , Ly- δ ; C IV 1548,1550; C III 977; Si III 1206; Si IV 1393,1402
$z_{15} = 2.9617$	Ly- α , Ly- β , Ly- γ , Ly- δ ; C III 977; C IV 1548,1550(+Si II 1526 DLA); N II 1083; N III 989; Al III 1854; Si II 1190; Si III 1206
$z_{16} = 2.9659$	Ly- α , Ly- β , Ly- γ (+Si II 1526 z_4), Ly- δ , Ly- ϵ ; C III 977; C IV 1548; N III 989(+L11-0P2); Si III 1206
$z_{17} = 2.9792$	Ly- α , Ly- β , Ly- γ ; C II 1036(+Ly- β DLA); C III 977; C IV 1548,1550;
$z_{18} = 3.0217$	Ly- α (+Ly- α DLA); C III 977(+O I 976 DLA); C IV 1548,1550; N II 1083; N III 989; Si IV 1393,1402
$z_{19} = 3.0632$	Ly- α , Ly- β , Ly- γ (+Ly- β z_{13}), Ly- δ (+N III 989 z_{14}); C III 977; C IV 1548,1550

REFERENCES

- Abgrall, H., & Roueff, E. 1989, *A&AS*, 79, 313
- Aitken, A. C. 1934, *Proceedings of the Royal Society Edinburgh A*, 55, 42
- Andreani, P., Cimatti, A., Loinard, L., & Röttgering, H. 2000, *A&A*, 354, L1
- Bahcall, J. N., & Wolf, R. A. 1968, *ApJ*, 152, 701
- Ballester, P., Modigliani, A., Boitquin, O., Cristiani, S., Hanuschik, R., Kaufer, A., & Wolf, S. 2000, *The Messenger*, 101, 31
- Barvainis, R., Maloney, P., Alloin, D., & Antonucci, R. 1997, *ApJ*, 484, 695
- Bendat, J. S., & Piersol, A. G. 1971, *Random data: Analysis and measurement procedures* (J. Wiley & Sons, Inc.: New York)
- Bergeson, S. D., & Lawler, J. E. 1993, *ApJ*, 408, 382
- Black, J. H., & Dalgarno, A. 1976, *ApJ*, 203, 132
- Black, J. H., & Dalgarno, A. 1977, *ApJS*, 34, 405
- Brown, R. L., & Van den Bout, P. A. 1992, *ApJ*, 397, L19
- Burles, S., Nollett, K. M., Truran, J. N., & Turner, M. S. 1999, *PhRvL*, 82, 4176
- Cardelli, J. A., & Savage, B. D. 1995, *ApJ*, 452, 275
- Carilli, C. L., Menten, K. M., & Yun, M. S. 1999, *ApJ*, 521, L25
- Carruthers, G. 1970, *ApJ*, 161, L81
- Centurión, M., Bonifacio, P., Molaro, P., & Vladilo, G. 1998, *ApJ*, 509, 620
- Centurión, M., Bonifacio, P., Molaro, P., & Vladilo, G. 2000, *ApJ*, 536, 540
- Charro, E., & Martín, I. 2000, *ApJS*, 126, 551
- de Boer, K. S., Richter, P., Bomans, D. J., Heithausen, A., & Koornneef, J. 1998, *A&A*, 338, L5
- Dessauges-Zavadsky, M., D'Odorico, S., McMahon, R. G., Molaro, P., Ledoux, C., Péroux, C., & Storrie-Lombardi, L. J. 2001, *A&A*, 370, 426
- D'Odorico, S., Cristiani, S., Dekker, H., Hill, V., Kaufer, A., Kim, T., & Primas, F. 2000, in *Proc. of SPIE Vol. 4005, Discoveries and Research Prospects from 8- to 10-Meter-Class Telescopes*, ed. J. Bergeron (Bellingham: SPIE), 121
- D'Odorico, S., Dessauges-Zavadsky, M., & Molaro, P. 2001, *A&A*, 368, L1 (DDM)
- Downes, D., Neri, R., Wiklind, T., Wilner, D. J., & Shaver, P. A. 1999, *ApJ*, 513, L1
- Elitzur, M., & Watson, W. D. 1978, *A&A*, 70, 443
- Federman, S. R., Beideck, D. J., Schectman, R. M., & York, D. G. 1992, *ApJ*, 401, 367 to CLOUDY (Univ. of Kentucky, Dept. of Phys. and Astron., Internal Report; <http://www.pa.uky.edu/gary/cloudy/>)
- Field, G. B., Sommerville, W. B., & Dressler, K. 1966, *ARA&A*, 4, 207
- Flower, D. R. & Pineau des Forêts, G. 2000, *MNRAS*, 316, 901
- Foltz, C. B., Chaffee, F. H., & Black, J. H. 1988, *ApJ*, 324, 267
- Frayser, D. T. et al. 1999, *ApJ*, 514, L13
- Fuller, T. M., & Couchman, H. M. P. 2000, *ApJ*, 544, 6
- Galli, D., & Palla, F. 1998, *A&A*, 335, 403
- Ge, J., & Bechtold, J. 1997, *ApJ*, 477, L73
- Ge, J., & Bechtold, J. 1999, in *ASP Conf. Ser. 156, Highly Redshifted Radio Lines*, eds. C. L. Carilli, S. J. E. Radford, K. M. Menten, & G. I. Langston (San Francisco: ASP), 121
- Ge, J., Bechtold, J., & Kulkarni, V. P. 2001, *ApJ*, 547, L1
- Gould, R. J., & Salpeter, E. E. 1963, *ApJ*, 138, 393
- Grevesse, N., & Sauval A. J. 1998, *Space Sci. Rev.*, 85, 161

- Guilloteau, S., Omont, A., McMahon, R. G., Cox, P., & Petitjean, P. 1997, *A&A*, 328, L1
- Haardt, F., & Madau, P. 1996, *ApJ*, 461, 20
- Haiman, Z., Rees, M. J., & Loeb, A. 1997, *ApJ*, 476, 458
- Henry, R. B. C., & Worthey, G. 1999, *PASP*, 111, 919
- Henry, R. B. C., Edmunds, M. G., & Köppen, J. 2000, *ApJ*, 542, 978
- Hollenbach, D. J., Werner, M. W., & Salpeter, E. E. 1971, *ApJ*, 163, 165
- Hollenbach, D., & McKee, C. F. 1980, *ApJ*, 241, L47
- Howk, J. C., Sembach, K. R., Roth, K. C., & Kurk, J. W. 2000, *ApJ*, 544, 867
- Israelian, G., Rebolo, R., García López, R. J., Bonifacio, P., Molaro, P., Basri, G., & Shchukina, N. 2001, *ApJ*, 551, 833
- Iwata, I., Ohta, K., Nakanishi, K., Kohno, K., & McMahon, R. G. 2001, *PASJ*, in press, astro-ph/0107369
- Jenkins, E. B., & Peimbert, A. 1997, *ApJ*, 477, 265
- Jenkins, E. B., Woźniak, P. R., Sofia, U. J., Sonneborn, G., & Tripp, T. M. 2000, *ApJ*, 538, 275
- Jura, M. 1974, *ApJ*, 191, 375
- Jura, M. 1975a, *ApJ*, 197, 575
- Jura, M. 1975b, *ApJ*, 197, 581
- Kunth, D., Lequeux, J., Sargent, W. L. W., & Viallefond, F. 1994, *A&A*, 282, 709
- Launay, J. M., & Roueff, E. 1977a, *J. Phys. B*, 10, 879
- Launay, J. M., & Roueff, E. 1977b, *A&A*, 56, 289
- Ledoux, C., Petitjean, P., Bergeron, J., Wampler, E. J., & Srianand, R. 1998, *A&A*, 337, 51
- Linsky, J. L. 1998, *SSRv*, 84, 285
- Levshakov, S. A., & Varshalovich, D. A. 1985, *MNRAS*, 212, 517
- Levshakov, S. A., & Foltz, C. B. 1988, *Sov. Astron. Lett.* 14, 467
- Levshakov, S. A., Foltz, C. B., Chaffee, F. H., & Black, J. H. 1989, *AJ*, 98, 2052
- Levshakov, S. A., Chaffee, F. H., Foltz, C. B., & Black, J. H. 1992, *A&A*, 262, 385
- Levshakov, S. A., Kegel, W. H., & Takahara, F. 1998, *ApJ*, 499, L1
- Levshakov, S. A., Kegel, W. H., & Takahara, F. 1999a, *MNRAS*, 302, 707
- Levshakov, S. A., Takahara, F., & Agafonova, I. I. 1999b, *ApJ*, 517, 609
- Levshakov, S. A., Tytler, D., & Burles, S. 2000a, *Astron. Astrophys. Trans.*, 19, 385
- Levshakov, S. A., Molaro, P., Centurión, M., D'Odorico, S., Bonifacio, P., & Vladilo, G. 2000b, *A&A*, 361, 803
- Levshakov, S. A., Agafonova, I. I., & Kegel, W. H. 2000c, *A&A*, 360, 833
- Levshakov, S. A., Molaro, P., Centurión, M., D'Odorico, S., Bonifacio, P., & Vladilo, G. 2001, in *ESO/ST-ECF/STScI Conf. Proc., Deep Fields*, in press, astro-ph/0011470
- Lopez, S., Reimers, D., Rauch, M., Sargent, W. L. W., & Smette, A. 1999, *ApJ*, 513, 598
- Mather, J. C., Fixsen, D. J., Shafer, R. A., Mosier, C., & Wilkinson, D. T. 1999, *ApJ*, 512, 511
- Mathis, J. S., Mezger, P. G., & Panagia, N. 1983, *A&A*, 128, 212
- Meyer, S. L. 1975, *Data analysis for scientists and engineers* (J. Wiley & Sons, Inc.: New York)
- Meyer, D. M., & York, D. G. 1992, *ApJ*, 399, L121
- Meyer, D. M., Lanzetta, K. M., & Wolfe, A. M. 1995, *ApJ*, 451, L13
- Molaro, P., Bonifacio, P., Centurión, M., D'Odorico, S., Vladilo, G., Santin, P., & Di Marcantonio, P. 2000, *ApJ*, 541, 54
- Molaro, P., Levshakov, S. A., D'Odorico, S., Bonifacio, P., & Centurión, M. 2001a, *ApJ*, 549, 90

- Molaro, P., Levshakov, S. A., Dessauges-Zavadsky, M., & D'Odorico, S. 2001b, A&A, submit.
- Møller, P., & Warren, S. J. 1993, A&A, 270, 43
- Moos, H. W., et al. 2000, ApJ, 538, L1
- Morton, D. C. 1991, ApJS, 77, 119
- Morton, D. C., & Dinerstein, H. L. 1976, ApJ, 204, 1
- Netterfield, C. B. et al. 2001, ApJ, submit., astro-ph/0104460
- Nishimura, S. 1968, Ann. Tokyo Astr. Obs., 2d ser., 11, 33
- Ohta, K., Yamada, T., Nakanishi, K., Kokno, K., Akiyama, M., & Kawabe, R. 1996, Nature, 382, 426
- Omont, A., Petitjean, P., Guilloteau, S., McMahon, R. G., Solomon, P. M., & Pecontal, E. 1996, Nature, 382, 428
- Osmer, P. S., & Smith, M. G. 1980, ApJS, 42, 333
- Papadopoulos, P. P., Röttgering, H. J. A., van der Werf, P. P., Guilloteau, S., Omont, A., van Breugel, W. J. M., & Tilanus, R. P. J. 2000, ApJ, 528, 626
- Papadopoulos, P. P., Ivison, R., Carilli, C., & Lewis, G. 2001, Nature, 409, 58
- Péquignot, D., Petitjean, P., & Boisson, C. 1991, A&A, 251, 680
- Petitjean, P., Srianand, R., & Ledoux, C. 2000, A&A, 364, 26
- Pettini, M., Smith, L. J., Hunstead, R. W., & King, D. L. 1994, ApJ, 426, 79
- Pettini, M., Ellison, S. L., Steidel, C. C., & Bowen, D. V. 1999, ApJ, 510, 576
- Pettini, M., Ellison, S. L., Steidel, C. C., Shapley, A. E., & Bowen, D. V. 2000, ApJ, 532, 65
- Pierre, M., Shaver, P. A., & Robertson, J. G. 1990, A&A, 235, 15
- Press, W. H., Teukolsky, S. A., Vetterling, W. T., & Flannery, B. P. 1992, Numerical Recipes (Cambridge, UK: Cambridge Univ. Press)
- Prochaska, J. X., & Wolfe, A. 1999, ApJS, 121, 369
- Raassen, A. J. J., & Uylings, P. H. M. 1998, J. Phys. B, 31, 3137
- Richter, P., et al. 1998, A&A, 338, L9
- Savage, B. D., Drake, J. F., Budich, W., & Bohlin, R. C. 1977, ApJ, 216, 291
- Shull, J. M., & Beckwith, S. 1982, ARA&A, 20, 163
- Shull, J. M., et al. 2000, ApJ, 538, L73
- Silva, A. I., & Viegas, S. M. 2001, MNRAS, in press, astro-ph/0012323
- Sofia, V. J., & Jenkins, E. B. 1998, ApJ, 499, 951
- Solomon, P. M., Downes, D., & Radfort, S. J. E. 1992, ApJ, 398, L29
- Spitzer, L., Jr., & Cochran, W. D. 1973, ApJ, 186, L23
- Spitzer, L., Jr., & Zweibel, E. G. 1974, ApJ, 191, L127
- Spitzer, L., Jr., Cochran, W. D., & Hirshfeld, A. 1974, ApJS, 28, 373
- Spitzer, L., Jr., & Jenkins, E. B. 1975, ARA&A, 13, 133
- Spitzer, L., Jr., & Fitzpatrick, E. L. 1993, ApJ, 409, 299
- Srianand, R., & Petitjean, P. 1998, A&A, 335, 33
- Srianand, R., Petitjean, P., & Ledoux, C. 2001, Nature, 408, 931
- Tikhonov, A. N., & Arsenin, V. A. 1977, Solution of Ill-Posed Problems (Washington, DC: Winston & Sons)
- Timmes, F. X., Woosley, S. E., & Weaver, T. A. 1995, ApJS, 98, 617
- Tomkin, J., Woolf, V. M., Lambert, D. L., & Lemke, M. 1995, AJ, 109, 2204
- Turner, J., Kirby-Docken, K., & Dalgarno, A. 1977, ApJS, 35, 281

Tytler, D., O'Meara, J. M., Suzuki, N., & Lubin,
D. 2000, PhR, 333, 409

Vidal-Madjar, A., et al. 2000, ApJ, 538, L77

Vladilo, G. 1998, ApJ, 493, 583

Williger, G. M., Carswell, R. F., Webb, J. K., Bok-
senberg, A., & Smith, M. G. 1989, MNRAS,
237, 635

Wolfe, A. M., & Briggs, F. H. 1981, ApJ, 248, 460

Wolfe, A. M., et al. 1994, ApJ, 435, 101

Wolfe, A. M., Lanzetta, K. M., Foltz, C. B., &
Chaffee, F. H. 1995, ApJ, 454, 698

Fig. 1.— A portion of the normalized spectrum of Q0347–3819 in the region of a few H₂ lines from the Lyman and Werner bands (labels ‘L’ and ‘W’, respectively) identified in the $z_{\text{abs}} = 3.025$ damped Ly α system. The noise level is indicated by the dashed curve at the bottom of the panel. The general continuum was estimated by using a polynomial fit to the ‘continuum windows’ in all spectral range spanning about 1200 Å. In cases where the curvature of the QSO continuum at $z = 3.025$ is strong, the uncertainty in the local continuum level may be dominated by uncertainties in the fitting procedure.

Fig. 2.— Confidence regions in the ‘ $\chi^2 - b$ ’ plane calculated from the simultaneous fit of the H₂ lines from Table 1 as described in the text. The parabola vertex corresponds to the most probable value of $b = 2.80 \text{ km s}^{-1}$.

Fig. 3.— Curves of growth for 31 H₂ lines ($J = 0, 1, 2, 3, 4,$ and 5 ; see Table 1) in the $z_{\text{abs}} = 3.025$ molecular cloud toward Q0347–3819. Most probable Doppler parameter is $b_{\text{H}_2} = 3 \text{ km s}^{-1}$. Curves with $b = 2 \text{ km s}^{-1}$ and 4 km s^{-1} restrict the 1σ confidence region for b_{H_2} .

Fig. 4.— Confidence regions in the ‘ $\chi^2 - \text{Log}N(J)$ ’ planes calculated from the simultaneous fits of the H₂ lines arising from the same J levels. The parabola vertexes correspond to the most probable values of $N(0) = 1.90 \times 10^{13} \text{ cm}^{-2}$, $N(1) = 1.60 \times 10^{14} \text{ cm}^{-2}$, $N(2) = 5.40 \times 10^{13} \text{ cm}^{-2}$, $N(3) = 1.22 \times 10^{14} \text{ cm}^{-2}$, $N(4) = 2.60 \times 10^{13} \text{ cm}^{-2}$, and $N(5) = 2.90 \times 10^{13} \text{ cm}^{-2}$.

Fig. 5.— H₂ absorption features associated with the $z_{\text{abs}} = 3.025$ damped Ly α system toward Q0347–3819 (normalized intensities are shown by dots with 1σ error bars). The zero radial velocity is fixed at $z_{\text{H}_2} = 3.024855$. Smooth lines are the synthetic H₂ spectra calculated for the mean physical parameters (see text). Possible blends with lines from the $z_{\text{abs}} = 3.025$ system are shown without indicating redshift, whereas blends with lines from other systems are indicated by ionic species with redshifts in accord with the list in Appendix B. H₂ profiles disturbed by the Ly- α forest absorption are also included.

Fig. 6.— Same as Figure 5.

Fig. 7.— Spectral regions including the H₂ transitions of the Lyman and Werner bands (labeled in panels) in the $z = 3.024637$ absorber in the direction of Q0347–3819. The lowest panel presents the result of a stacking. The 3σ upper limit of 0.6 mÅ was calculated for a 12 km s^{-1} window centered at $v = 0 \text{ km s}^{-1}$.

Fig. 8.— Population of the low rotational levels of H₂ in the $z_{\text{abs}} = 3.025$ damped Ly α system toward Q0347–3819. Error bars for 1σ deviations are shown. The negative inverse slope of the best-fit straight dotted line indicates the excitation temperature of about 800 K.

Fig. 9.— Relation between H₂ fractional abundance f_{H_2} plotted on a logarithmic scale and relative heavy element depletion in DLAs. The solid line corresponds to the linear law: $\log f_{\text{H}_2} \simeq -6.1 [\text{Cr}/\text{Zn}] - 7.9$, obtained for the five measurements of f_{H_2} we know (DLAs # 5, 8, 12, 13 and 14). The filled circles correspond to $[\text{Cr}/\text{Zn}]$ and the open ones to $[\text{Fe}/\text{Zn}]$. See Table 2 for references.

Fig. 10.— Metal absorption features associated with the $z_{\text{abs}} = 3.025$ DLA toward Q0347–3819 (normalized intensities are shown by dots with 1σ error bars). The zero radial velocity is fixed at $z_{\text{abs}} = 3.024855$. The smooth lines are the synthetic spectra convolved with the instrumental resolution of $\text{FWHM} = 7.0 \text{ km s}^{-1}$. Two groups of lines (H I, C II, C II*, N I, O I, Si II, P II, Ar I, Zn II, and Fe II, Cr II) are fitted simultaneously to the observed profiles or to their portions marked by horizontal lines which also indicate pixels involved in the optimization procedure (the corresponding hydrogen profiles are shown in Figures 11 and 12). For Zn II and Cr II composite stacked spectra are shown. Two absorption features at $\Delta v \simeq 17 \text{ km s}^{-1}$ (Zn II) and $\Delta v \simeq 6 \text{ km s}^{-1}$ (Cr II) are telluric lines. Possible blends with lines from other systems are indicated by ionic species with redshifts in accord with the list in Appendix B.

Fig. 11.— Same as Figure 10 but for the hydrogen and deuterium lines. For the Ly- α line only a portion of its blue wing free of the forest absorptions is shown. The blue wing of Ly- β is contaminated by the forest absorption. The deuterium absorption seen in Ly-8, Ly-10 and Ly-12 is shown zoomed in Figure 12. The corresponding D/H ratio is equal to 3.75×10^{-5} .

Fig. 12.— Same as Figure 11 to show details of the H+D (thick lines) and D (thin lines) profiles.

Fig. 13.— Radial velocity distributions $p(v)$ for the models adopted in the present paper (solid and dotted curves) and, for comparison, $p(v)$ from DDM (dashed curve). The difference in shapes of $p(v)$ leads to the difference in the estimations of D/H: $(2.24 \pm 0.67) \times 10^{-5}$ (DDM) and $(3.75 \pm 0.25) \times 10^{-5}$ (see Figure 14). The intense and narrow spike at $\Delta v \simeq 0 \text{ km s}^{-1}$ was revealed from the analysis of the H₂ lines.

Fig. 14.— Confidence regions in the ‘H I – D/H’ plane calculated from the simultaneous fit of the H I and metal lines shown in Figures 10 and 11 when the other best-fitting parameters of the adopted model are fixed. The contours represent 68.3% (inner) and 95.4% (outer) confidence levels. The cross marks the point of maximum likelihood for the adopted model ($\chi_{\min}^2 = 1.22, \nu = 545$).

Fig. 15.— Fractional ionization ratios $\Upsilon_{\text{Si II}}/\Upsilon_{\text{C II}}$ and $\Upsilon_{\text{Fe II}}/\Upsilon_{\text{C II}}$ versus the ionization parameter U in the case of a soft, starlight background (solid curves) and a hard, QSO-dominated ionizing field (dashed curves). Similarity of the line profiles of a pair of ions requires the fractional ionization ratio to be constant for different U .

Fig. 16.— Autocorrelation functions (ACF) of the intensity fluctuations in the continuum between $\lambda 6790 \text{ \AA}$ and $\lambda 6820 \text{ \AA}$ in the UVES spectrum of Q0347–3819 before and after randomization (histograms in panels **a** and **b**, respectively). The smooth curves show the ACFs of the first order autoregression process with correlation lengths indicated by ξ (see text for more details).

TABLE 1
H₂ LINES AT $z_{\text{abs}} = 3.025$ TOWARD Q0347-3819

J	Line	$\langle\lambda\rangle$, Å	$\sigma_{\langle\lambda\rangle}$, Å	W_{λ} , mÅ	$\sigma_{W_{\lambda}}$, mÅ	z	σ_z	
0	L3-0R ^a	4277.96	0.09	6.7	4.4	3.02486	0.00009	
	L7-0R ^{a,b}	4076.44	0.06	25.8	5.7	3.02485	0.00006	
1	W2-0Q ^b	3888.38	0.03	83.9	4.4	3.02487	0.00003	
	W3-0Q ^b	3813.22	0.05	55.7	7.2	3.02484	0.00005	
	L1-0P ^b	4403.42	0.04	25.4	4.1	3.02486	0.00004	
	L3-0R ^b	4280.27	0.03	65.6	3.8	3.02485	0.00002	
	L3-0P ^{a,b}	4284.89	0.04	24.2	4.2	3.02486	0.00004	
	L7-0R ^b	4078.95	0.03	76.4	4.8	3.02485	0.00003	
	L10-0P ^b	3955.77	0.04	46.8	5.0	3.02484	0.00004	
	L14-0P ^{a,b}	3813.61	0.09	24.6	7.2	3.02484	0.00009	
2	W0-0R ^{a,b}	4061.19	0.05	34.4	5.5	3.02488	0.00005	
	W0-0Q ^{a,b}	4068.87	0.04	50.7	6.7	3.02484	0.00004	
	W0-0P ^b	4073.85	0.09	10.3	4.1	3.02488	0.00009	
	W1-0Q ^b	3976.45	0.04	36.6	4.4	3.02487	0.00004	
	L3-0R ^{a,b}	4286.44	0.06	14.9	4.7	3.02485	0.00006	
	L3-0P ^b	4294.12	0.07	12.6	3.9	3.02485	0.00007	
	L4-0R ^{a,b}	4232.14	0.05	24.9	5.0	3.02487	0.00005	
	L5-0R ^{a,b}	4180.57	0.04	32.2	4.4	3.02485	0.00004	
3	W0-0Q ^b	4075.88	0.03	65.7	5.0	3.02485	0.00003	
	L2-0R ^b	4353.77	0.03	36.1	4.6	3.02488	0.00003	
	L2-0P ^a	4365.17	0.07	8.6	5.7	3.02481	0.00007	
	L3-0R ^b	4296.43	0.03	51.4	4.6	3.02484	0.00003	
	L3-0P ^{a,b}	4307.18	0.05	22.0	4.5	3.02487	0.00005	
	L4-0R ^b	4252.15	0.03	61.1	5.4	3.02486	0.00003	
	L4-0P ^a	4252.14	0.09	8.4	6.0	3.02486	0.00008	
	L6-0R ^b	4141.54	0.03	60.3	4.6	3.02487	0.00003	
	L7-0P ^b	4103.35	0.05	32.2	4.0	3.02484	0.00005	
	L8-0P ^{a,b}	4058.61	0.05	30.1	5.5	3.02484	0.00005	
	L12-0R ^{a,b}	3894.77	0.04	49.0	6.2	3.02488	0.00005	
4	L15-0R ^{a,b}	3795.31	0.08	20.8	5.0	3.02486	0.00008	
	L4-0P ^{a,b}	4268.64	0.05	24.1	5.9	3.02482	0.00005	
	L8-0P ^a	4074.21	0.09	8.6	5.0	3.02484	0.00009	
	5	W1-0Q ^{a,b}	4004.44	0.06	25.7	5.4	3.02489	0.00006
		L7-0P ^{a,b}	4138.55	0.10	8.5	4.7	3.02484	0.00010
	L12-0R ^{a,b}	3923.76	0.08	13.9	4.4	3.02484	0.00008	

NOTE.—^a Lines are used in the Voigt-fitting procedure to estimate the broadening b -parameter. ^b Lines are used in Figure 3.

TABLE 2
MOLECULAR HYDROGEN AND METAL ABUNDANCE MEASUREMENTS IN DLAs

#	QSO	z_{abs}	[Cr/Zn]	[Fe/Zn]	$\log N(\text{H I})$	$\log N(\text{H}_2)$	$\log f_{\text{H}_2}$
1	Q1328+307	0.692	-0.44 ± 0.10^a	—	21.28 ± 0.10^a	$< 15.70^b$	< -5.28
2	Q0454+039	0.860	0.14 ± 0.12^c	0.01 ± 0.12^c	20.69 ± 0.06^c	$< 16.38^b$	< -4.01
3	Q0935+417	1.373	-0.10 ± 0.16^d	-0.27 ± 0.15^d	20.40 ± 0.09^d	$< 16.40^b$	< -3.70
4	Q1157+014	1.944	—	-0.42 ± 0.11^e	21.80 ± 0.10^f	$< 14.71^e$	< -6.79
5	Q0013-004	1.973	$< -0.95^g$	$-1.10 \pm 0.13^{g,h}$	20.70 ± 0.05^i	19.84 ± 0.10^i	-0.66 ± 0.10
6	Q0458-020	2.040	-0.36 ± 0.05^j	-0.46 ± 0.07^j	21.65 ± 0.09^g	$< 15.90^b$	< -5.45
7	Q0100+130	2.309	-0.12 ± 0.05^j	-0.22 ± 0.06^j	21.40 ± 0.05^k	$< 15.70^b$	< -5.40
8	Q1232+082	2.338	—	$-0.86 \pm 0.13^{l,m}$	20.90 ± 0.10^m	17.18 ± 0.10^m	-3.42 ± 0.14
9	Q0841+129	2.374	$-0.12 \pm 0.08^{e,j}$	-0.29 ± 0.08^e	20.95 ± 0.09^j	$< 14.67^e$	< -5.98
10	Q0112+029	2.423	-0.75 ± 0.18^g	—	20.95 ± 0.10^g	$< 16.00^b$	< -4.65
11	Q1223+178	2.466	$-0.27 \pm 0.14^{g,e}$	-0.21 ± 0.11^e	21.52 ± 0.10^e	$< 14.30^e$	< -6.92
12	Q0528-250	2.811	-0.46 ± 0.14^n	$-0.46 \pm 0.12^{n,o}$	$21.35 \pm 0.10^{u,p}$	$16.77 \pm 0.09^{q,o}$	-4.28 ± 0.13
13	Q0347-382	3.025	-0.37 ± 0.06^r	-0.19 ± 0.06^r	20.626 ± 0.005^r	14.613 ± 0.022^r	-5.71 ± 0.02
14	Q0000-262	3.390	0.06 ± 0.07^t	0.03 ± 0.07^t	21.41 ± 0.08^j	$13.94 \pm 0.06^{v,w}$	-7.17 ± 0.13

NOTE.—Column densities $N(\text{H I})$ and $N(\text{H}_2)$ are given in cm^{-2} .
References: ^a Meyer & York (1992); ^b Ge & Bechtold (1999); ^c Pettini et al. (2000); ^d Meyer et al. (1995); ^e Petitjean et al. (2000); ^f Wolfe & Briggs (1981); ^g Pettini et al. (1994); ^h Centurion et al. (2000); ⁱ Ge & Bechtold (1997); ^j Prochaska & Wolfe (1999); ^k Wolfe et al. (1994); ^l Ge et al. (2001); ^m Srianand et al. (2001); ⁿ Lu et al. (1996); ^o Srianand & Petitjean (1998); ^p Møller & Warren (1993); ^q Levshakov & Varshalovich (1985); ^r this paper; ^t Molaro et al. (2000); ^u Levshakov & Foltz (1988); ^v Levshakov et al. (2000); ^w Levshakov et al. (2001)

TABLE 3
 COLUMN DENSITIES AND RELATIVE ABUNDANCES IN THE H₂-BEARING CLOUD AT $z_{\text{abs}} = 3.025$ TOWARD
 Q0347–3819

Ion	log N, cm ⁻²	(X/H) _⊙ ^b	[X/H]	[X/Zn]
H I	20.402 ± 0.006 ^a			
C I	< 11.6 ^{†,‡}			
C II*	13.354 ± 0.023			
C II	15.703 ± 0.024	-3.48 ± 0.06	-1.22 ± 0.06	0.29 ± 0.08
N I	14.664 ± 0.007	-4.08 ± 0.06	-1.66 ± 0.06	-0.15 ± 0.08
O I*	< 11.9 ^{†,‡}			
O I	16.410 ± 0.010	-3.17 ± 0.06	-0.82 ± 0.06	0.69 ± 0.08
Si II*	< 12.4 ^{†,‡}			
Si II	15.015 ± 0.013	-4.44 ± 0.05	-0.95 ± 0.02	0.56 ± 0.06
P II	12.779 ± 0.032	-6.44 ± 0.06	-1.18 ± 0.07	0.32 ± 0.09
Ar I	13.760 ± 0.020	-5.48 ± 0.04 ^c	-1.16 ± 0.05	0.35 ± 0.07
Cr II	11.698 ± 0.046	-6.31 ± 0.01	-2.39 ± 0.05	-0.89 ± 0.07
Fe II	13.690 ± 0.032	-4.50 ± 0.01	-2.21 ± 0.03	-0.71 ± 0.06
Zn II	11.565 ± 0.037	-7.33 ± 0.04	-1.51 ± 0.05	

NOTE.— ^a Indicated are the internal errors. [†] 1σ level; [‡] based on the Keck/HIRES data obtained by Prochaska & Wolfe (1999).
 References : ^b Grevesse & Sauval (1998); ^c from Sofia & Jenkins (1998).

TABLE 4

TOTAL COLUMN DENSITIES AND RELATIVE ABUNDANCES AT $z_{\text{abs}} = 3.025$ TOWARD Q0347-3819[†]

Ion	log N, cm ⁻²	(X/H) _⊙ ^d	[X/H]	[X/Zn]	[X/H] ^b	[X/H] ^c	[X/H] ^e
H I	20.626 ± 0.005 ^x						
C II	15.929 ± 0.024	-3.48 ± 0.06	-1.22 ± 0.06	0.29 ± 0.08		> -2.4	> -2.2
C II*	13.581 ± 0.024						
N I	14.890 ± 0.007	-4.08 ± 0.06	-1.66 ± 0.06	-0.15 ± 0.08	-2.1	-2.5	
O I	16.636 ± 0.011	-3.17 ± 0.06	-0.82 ± 0.06	0.68 ± 0.08	> -1.5	> -2.4	> -2.2
Si II	15.240 ± 0.013	-4.44 ± 0.05	-0.95 ± 0.02	0.56 ± 0.06	-1.2	> -1.9	-1.4
P II	13.005 ± 0.031	-6.44 ± 0.06	-1.18 ± 0.07	0.32 ± 0.09			
Ar I	13.986 ± 0.020	-5.48 ± 0.04 ^a	-1.16 ± 0.04	0.34 ± 0.07			
Cr II	12.441 ± 0.035	-6.31 ± 0.01	-1.88 ± 0.04	-0.37 ± 0.06			
Fe II	14.432 ± 0.009	-4.50 ± 0.01	-1.69 ± 0.01	-0.19 ± 0.06	-1.9	> -2.0	-1.7
Zn II	11.792 ± 0.036	-7.33 ± 0.04	-1.50 ± 0.05		< -0.8	< -1.2	

NOTE.—[†] Listed values were measured in the range $-50 \text{ km s}^{-1} \leq v \leq 20 \text{ km s}^{-1}$ (see Figure 10). ^x Indicated are the internal errors. References : ^a from Sofia & Jenkins (1998); ^b Centurión et al. (1998); ^c Ledoux et al. (1998); ^d Grevesse & Sauval (1998); ^e Prochaska & Wolfe (1999)

TABLE 5
H₂ TRANSITION PROBABILITIES AND EXCITATION RATE COEFFICIENTS FOR $\Delta J = 2$ TRANSITIONS
BETWEEN THE FIRST FIVE ROTATIONAL STATES

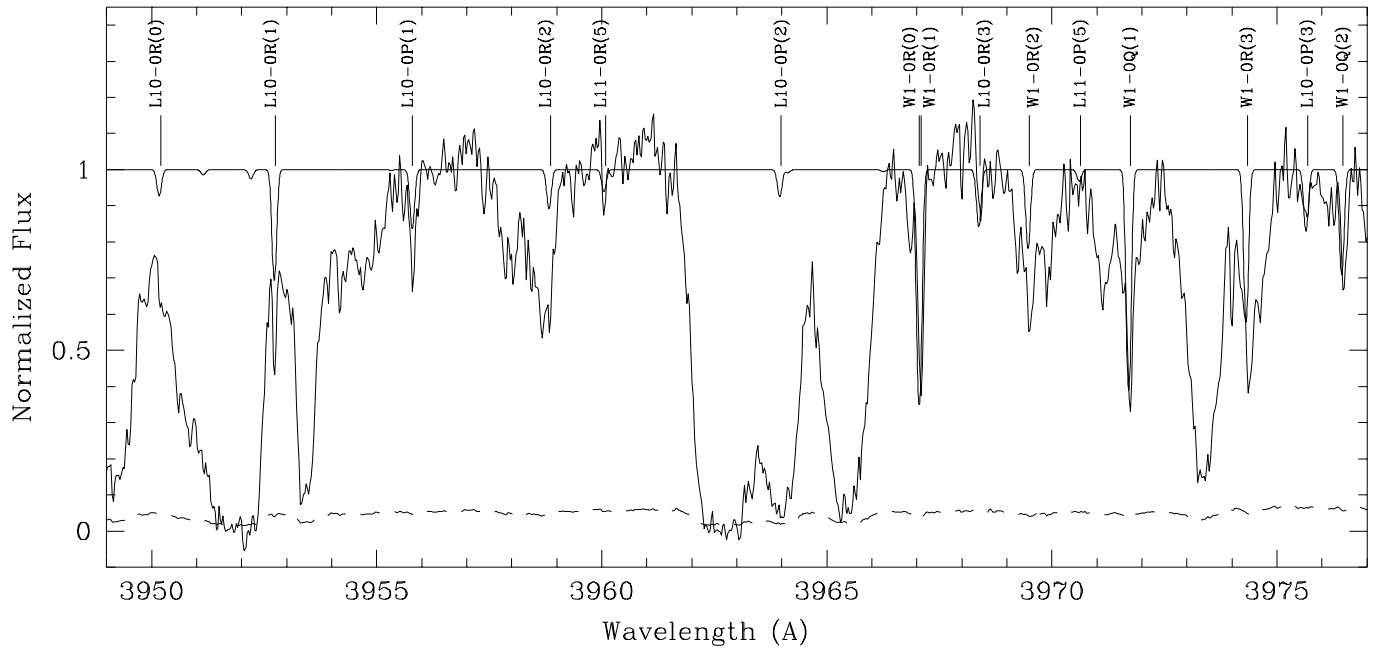
J	$A_{J+2 \rightarrow J} \left(\frac{1}{s} \right)^a$	$q_{J \rightarrow J+2}^{T=400K} \left(\frac{\text{cm}^3}{s} \right)^b$	$q_{J \rightarrow J+2}^{T=1000K} \left(\frac{\text{cm}^3}{s} \right)^b$	$q_{J \rightarrow J+2}^{T=1000K} \left(\frac{\text{cm}^3}{s} \right)^c$	$q_{J \rightarrow J+2}^{T=1000K} \left(\frac{\text{cm}^3}{s} \right)^d$
0	2.94(-11)	1.14(-11)	6.44(-11)	4.82(-11)	1.27(-10)
1	4.76(-10)	1.79(-12)	1.60(-11)	...	4.07(-11)
2	2.76(-9)	5.16(-13)	7.35(-12)	6.70(-12)	1.78(-11)
3	9.84(-9)	1.76(-13)	4.02(-12)	...	8.33(-12)

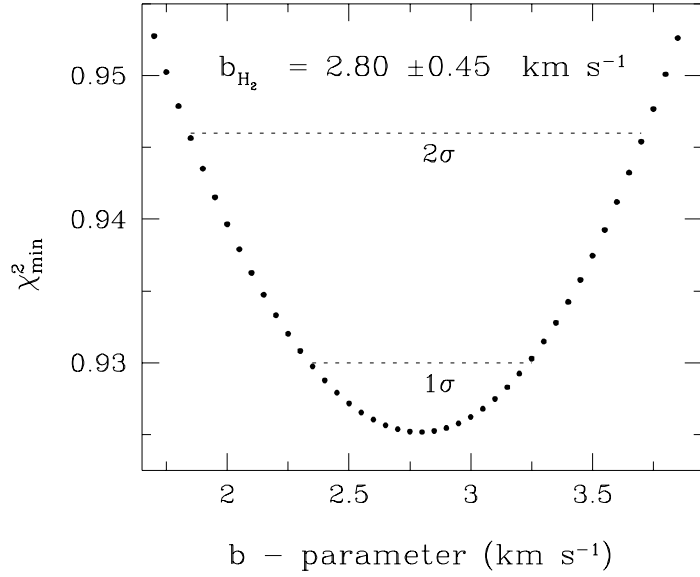
NOTE.—The negative numbers in parenthesis are the powets of ten. References : ^a Turner et al. (1977); ^b this paper; ^c Elitzur & Watson (1978); ^d Nishimura (1968)

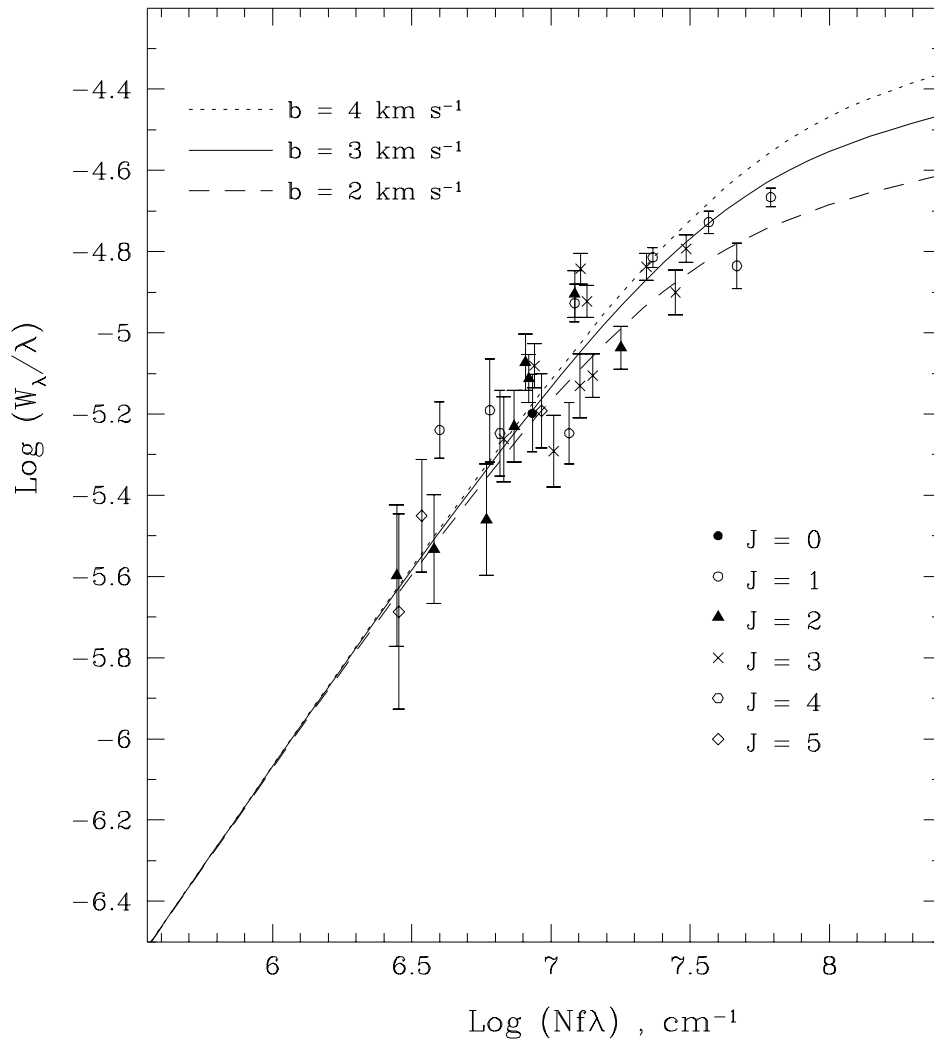
TABLE 6
COMPARISON OF THE MEAN VALUES AND THE STANDARD DEVIATIONS ESTIMATED BY THE MONTE CARLO (MC) AND $\Delta\chi^2$ METHODS IN CASE OF CORRELATED MEASUREMENTS

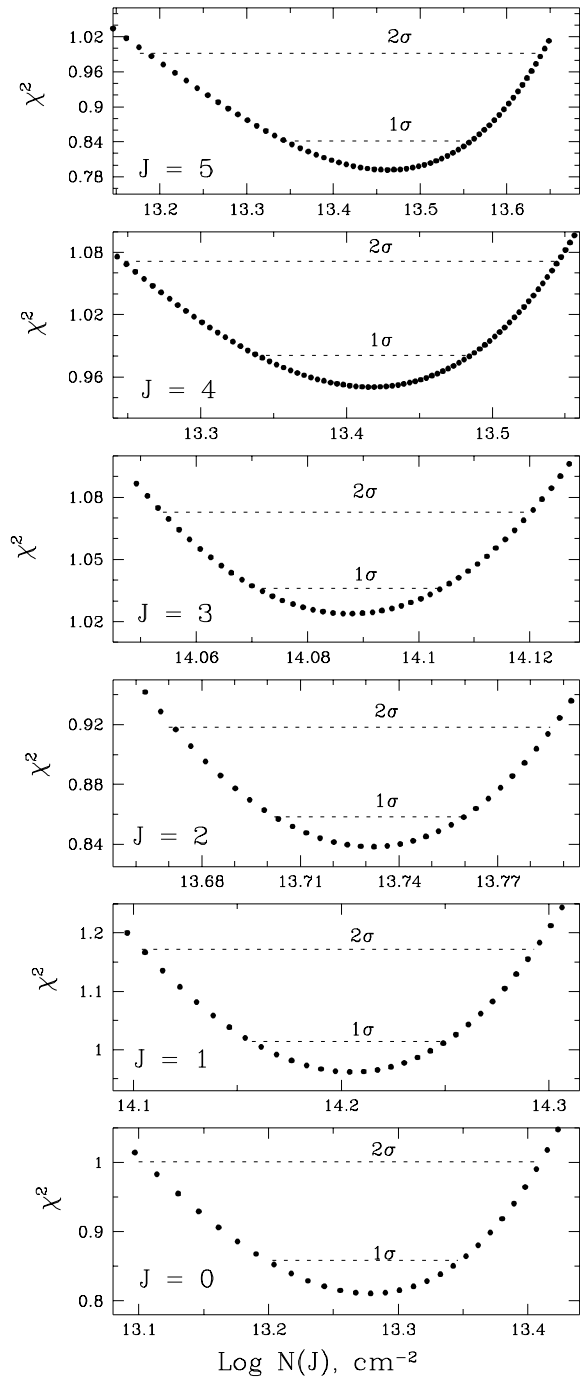
parameter, x	$\langle x \rangle_{\text{MC}}$	σ_{MC}	$\langle x \rangle_{\Delta\chi^2}$	$\sigma_{\Delta\chi^2}$
b^\ddagger , km s $^{-1}$	3.04	0.29	2.80	0.45
$N(\text{J}=0)$, cm $^{-2}$	1.90 $_{13}^\ddagger$	0.29 $_{13}$	1.90 $_{13}$	0.35 $_{13}$
$N(\text{J}=1)$, cm $^{-2}$	1.84 $_{14}$	0.13 $_{14}$	1.60 $_{14}$	0.18 $_{14}$
$N(\text{J}=2)$, cm $^{-2}$	5.39 $_{13}$	0.28 $_{13}$	5.40 $_{13}$	0.35 $_{13}$
$N(\text{J}=3)$, cm $^{-2}$	1.24 $_{14}$	0.07 $_{14}$	1.22 $_{14}$	0.05 $_{14}$
$N(\text{J}=4)$, cm $^{-2}$	2.35 $_{13}$	0.44 $_{13}$	2.60 $_{13}$	0.43 $_{13}$
$N(\text{J}=5)$, cm $^{-2}$	2.90 $_{13}$	0.53 $_{13}$	2.90 $_{13}$	0.70 $_{13}$

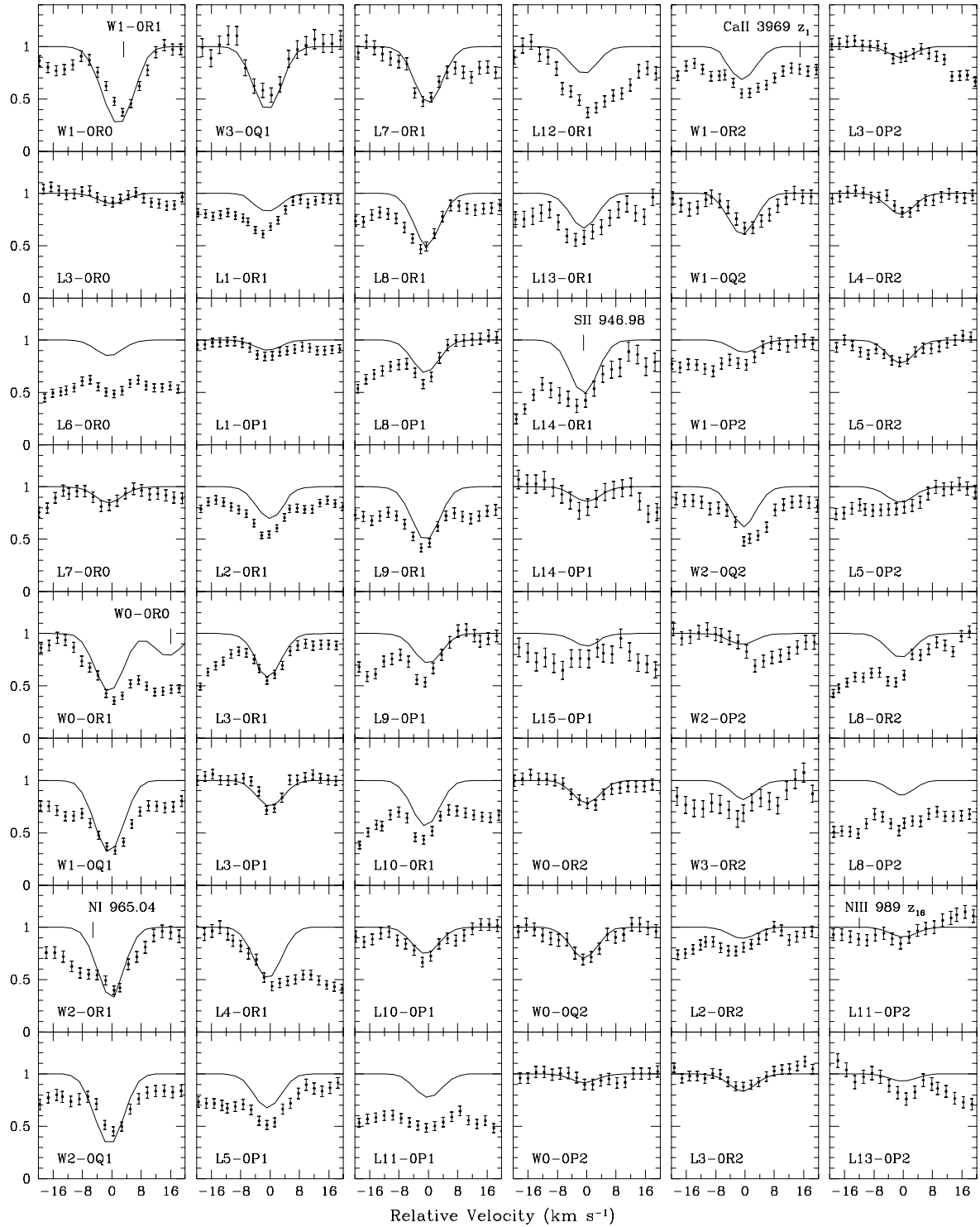
NOTE.— ‡ The H $_2$ column densities at different J levels and the corresponding broadening b parameter are listed in column (1). † Values like ' a_t ' mean $a \times 10^t$.

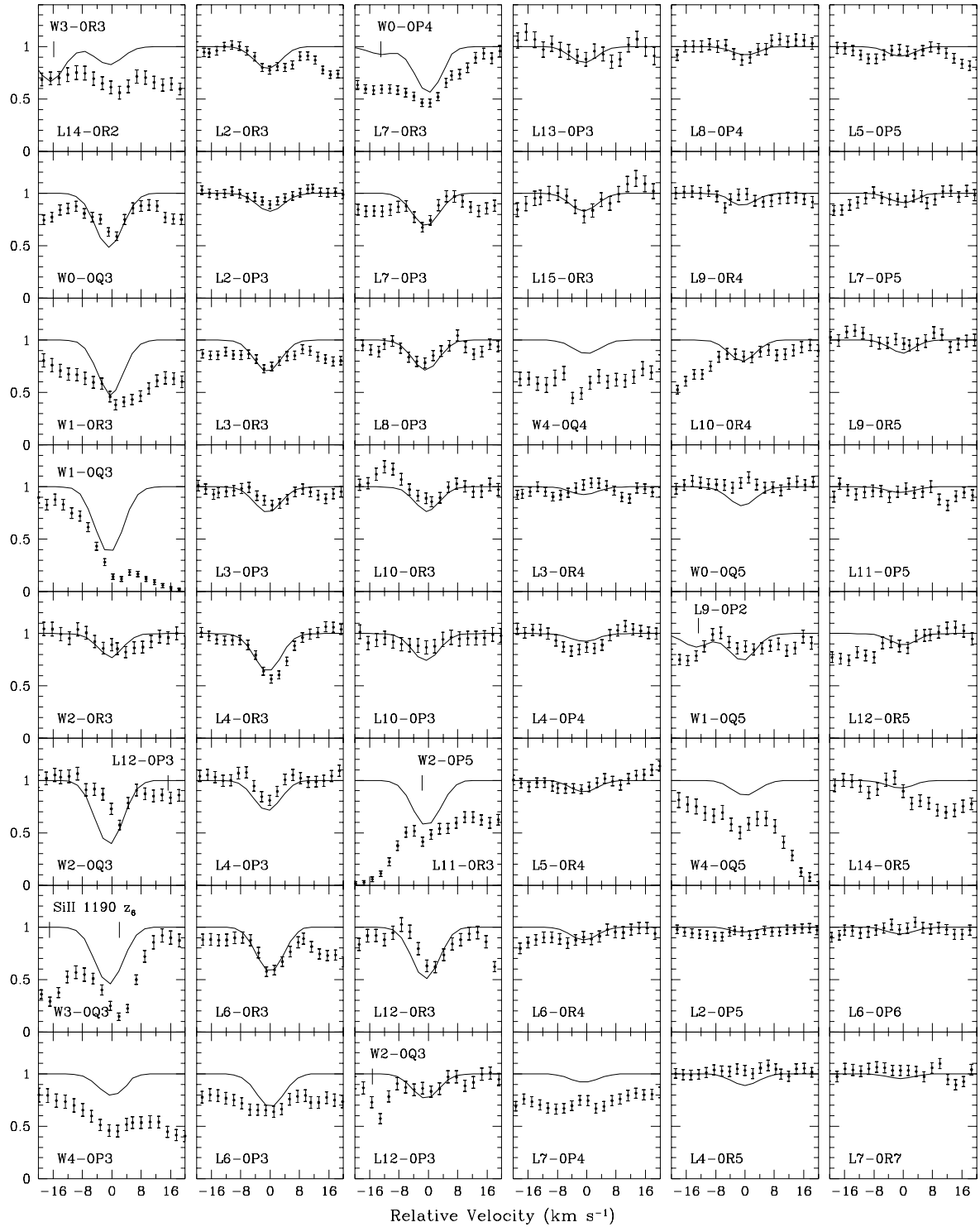


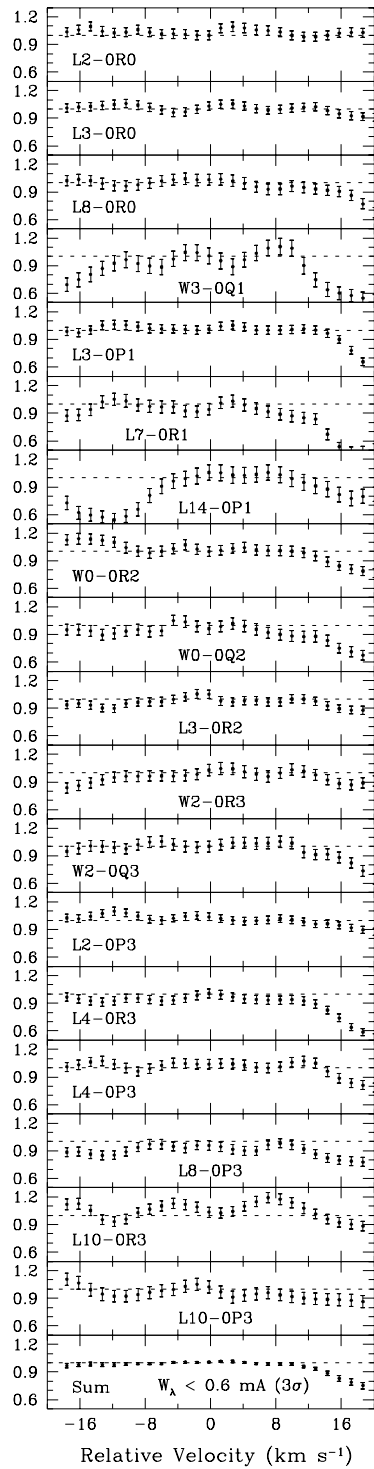


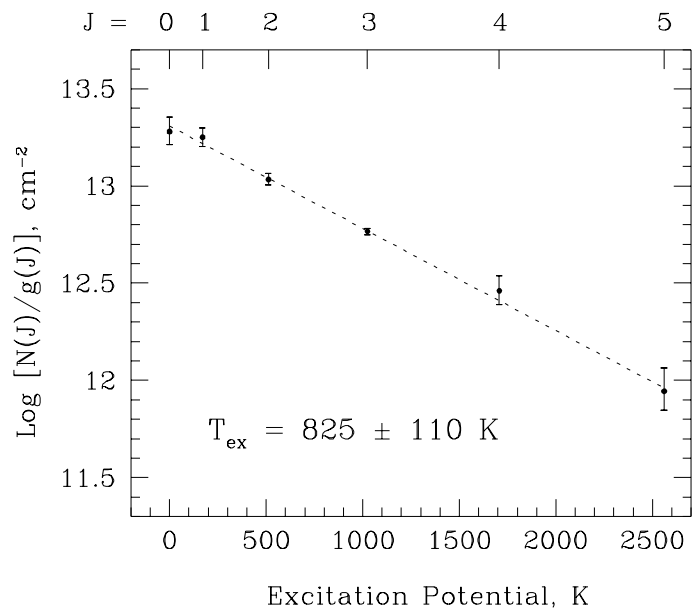


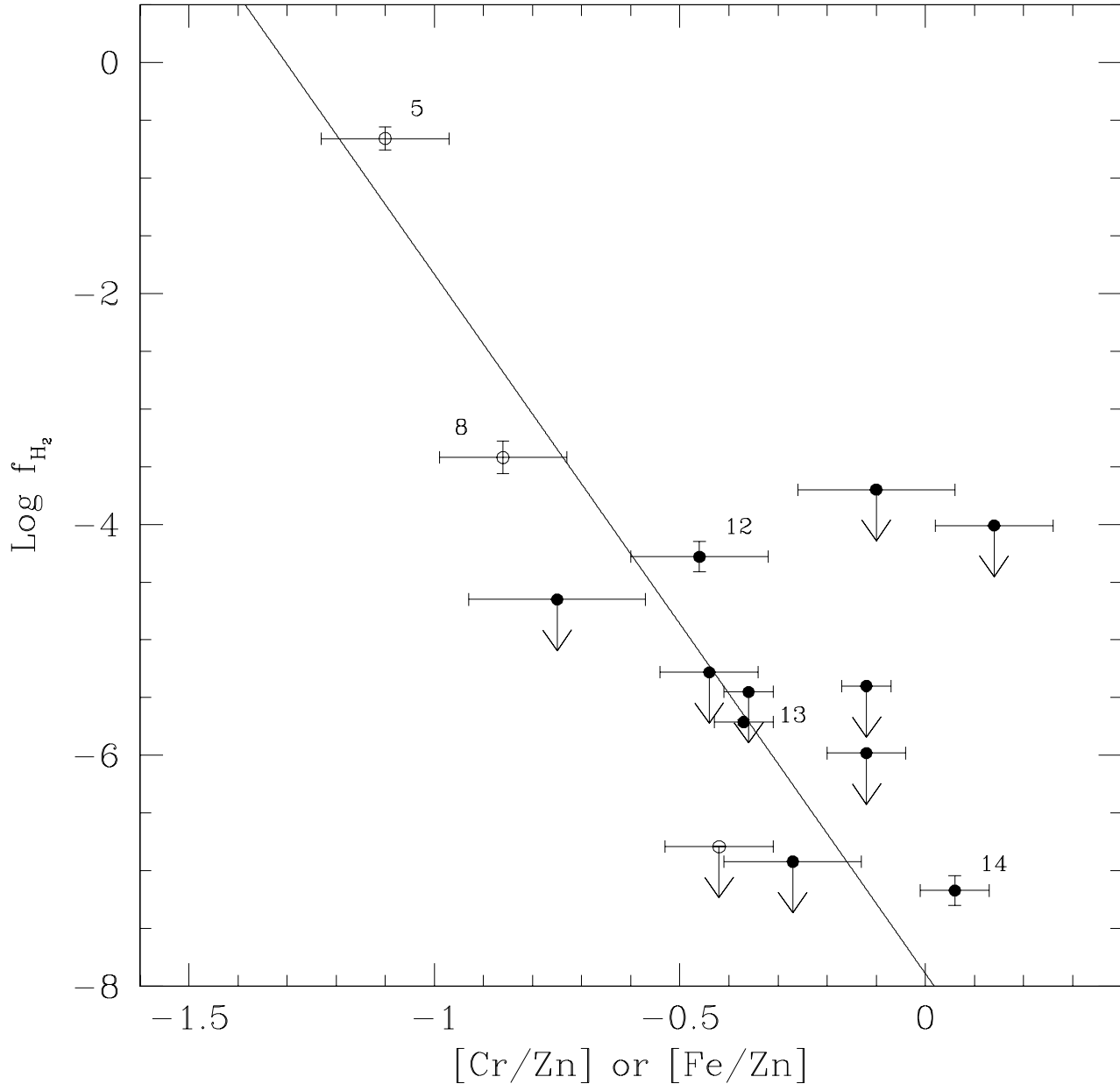


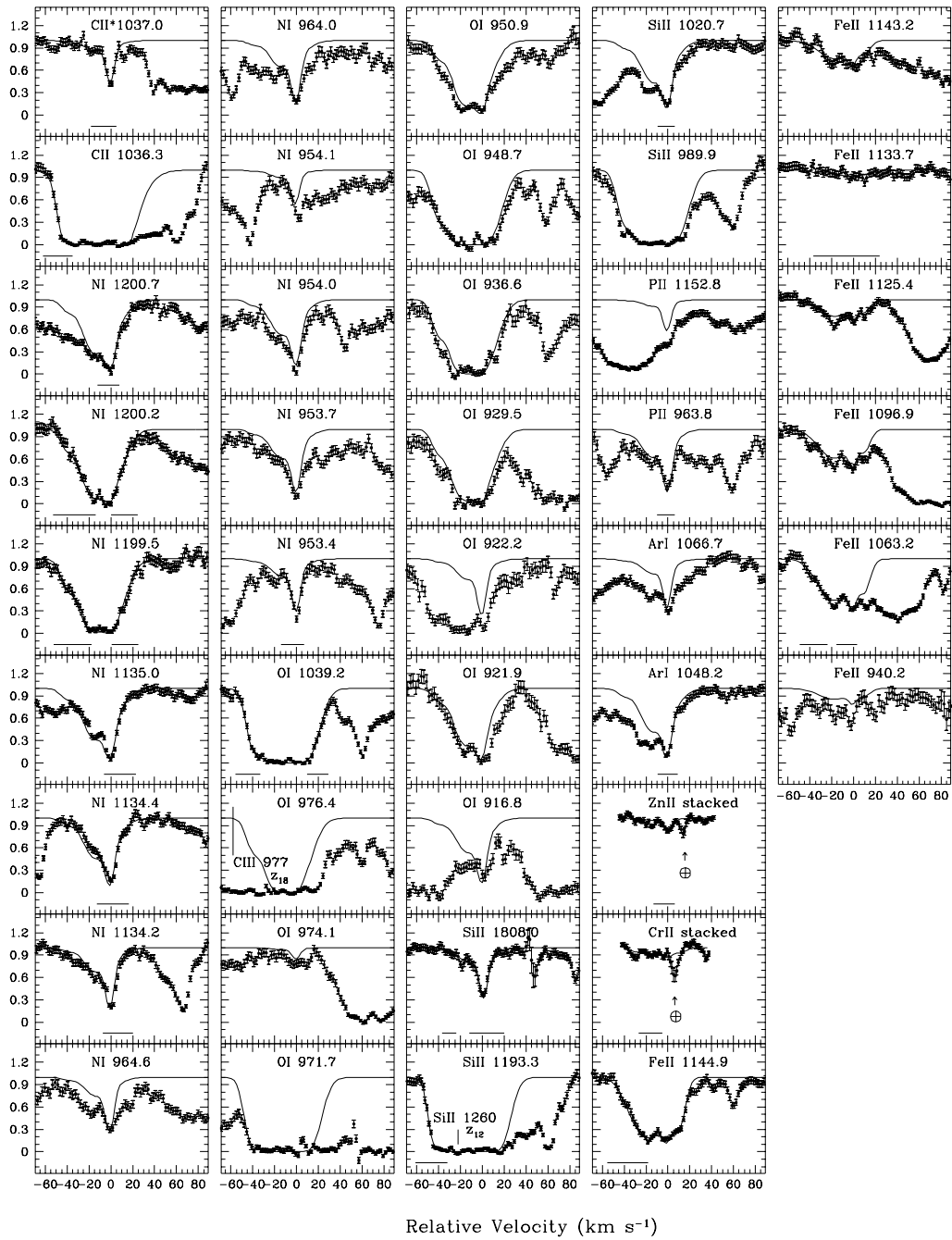


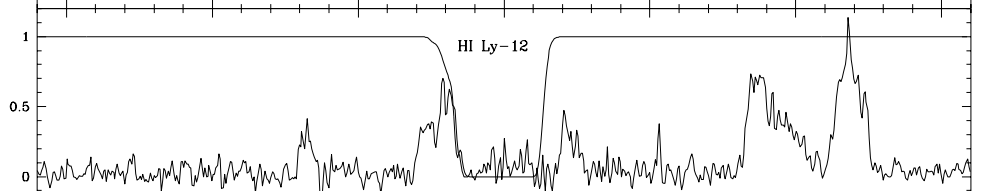
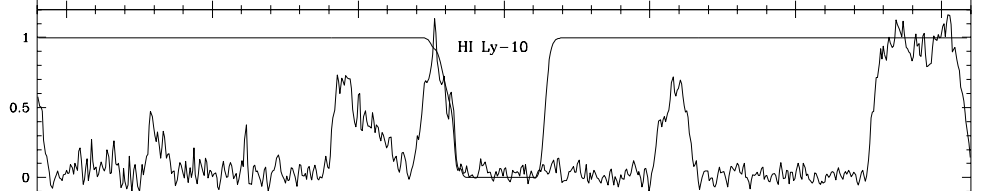
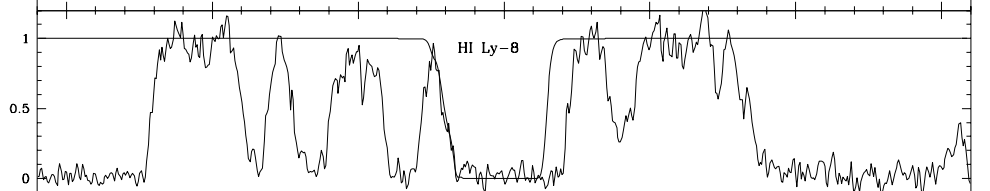
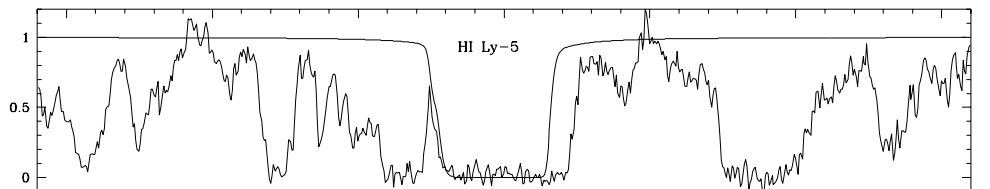
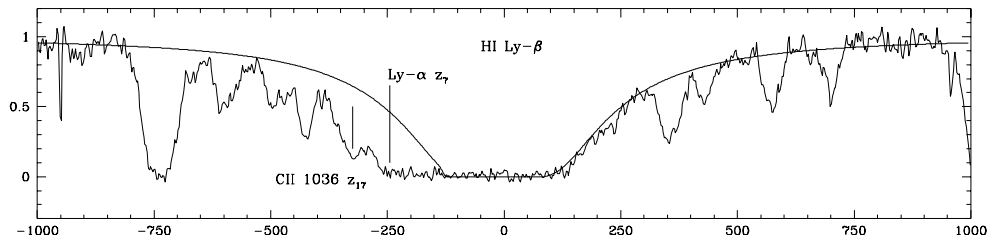
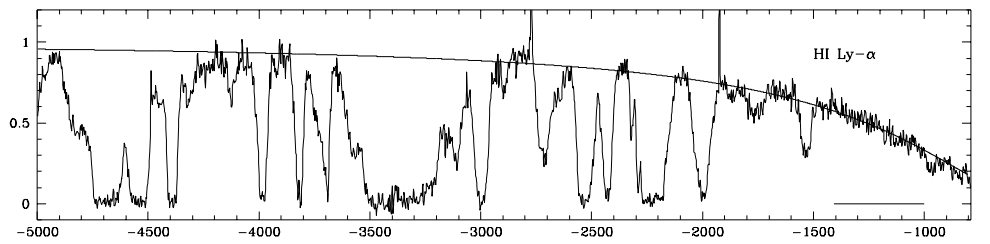












Relative Velocity (km s⁻¹)

